

The GeoCarb greenhouse gas retrieval algorithm: Simulations and sensitivity to sources of uncertainty.

Gregory R. McGarragh¹, Christopher W. O'Dell¹, Sean M. R. Crowell², Peter Somkuti², Eric B. Burgh³, and Berrien Moore III²

¹Cooperative Institute for Research in the Atmosphere, Colorado State University, Fort Collins, CO, USA

²University of Oklahoma, School of Meteorology, Norman, OK, USA

³Lockheed Martin Advanced Technology Center, Palo Alto, CA, USA

Correspondence: Gregory McGarragh (greg.mcgarraagh@colostate.edu)

Abstract. The Geostationary Carbon Cycle Observatory (GeoCarb) was selected as NASA's second Earth Venture Mission (EVM-2). The scientific objectives of GeoCarb ~~are~~ were to advance our knowledge of the carbon cycle, in particular, land-atmosphere fluxes of the greenhouse gases carbon dioxide (CO₂) and methane (CH₄), and the effects of these fluxes on the Earth's radiation budget. GeoCarb will retrieve ~~column-integrated amounts~~ column-integrated dry-air mole fractions of CO₂ (X_{CO_2}), CH₄ (X_{CH_4}) and CO (~~X_{CO}~~ X_{CO}), important for understanding tropospheric chemistry), in addition to Solar-Induced Fluorescence (SIF), from hyperspectral resolution measurements in the O₂ A-band at 0.76 μm, the weak CO₂ band at 1.6 μm, the strong CO₂ band at 2.06 μm, and a CH₄/CO band at 2.32 μm. Unlike its ~~polar-orbiting~~ predecessors (OCO-2/3, GOSAT-1/2, TROPOMI), GeoCarb ~~will be in a Geostationary~~ would have been in a geostationary orbit with a sub-satellite point centered over the Americas. This orbital configuration combined with its high spatial resolution imaging capabilities ~~will provide~~ would have provided an unprecedented view of these quantities on spatial and temporal scales accurate enough to resolve sources and sinks to improve land-atmosphere CO₂ and CH₄ flux calculations and reduce the uncertainty of these fluxes.

This paper will present a description of the GeoCarb instrument and the L2 retrieval algorithms which will be followed by simulation experiments to determine ~~a relatively comprehensive an~~ error budget for each target gas. Several sources of uncertainty will be explored including that from the instrument calibration parameters for radiometric gain, the instrument line shape (ILS), the polarization, and the geolocation pointing, in addition to ~~forward~~ model parameters including that from meteorology and spectroscopy although there are some other instrument related sources of uncertainty that are left out for this study, including that from "smile", the keystone effect, stray light, detector persistence, and scene inhomogeneity. The results indicate that the errors (1σ) are less than the instrument's multi-sounding precision requirements of 1.2 ppm, 10 ppb, and 12 ppb (10%), for X_{CO_2} , X_{CH_4} , and X_{CO} , respectively. In particular, when considering the sources of uncertainty separately and in combination (all sources included), we find overall RMS errors of 1.06 ppm for X_{CO_2} , 8.2 ppb for X_{CH_4} , and 2.5 ppb for X_{CO} , respectively. Additionally, we find that, as expected, errors in X_{CO_2} and X_{CH_4} are dominated by forward model and other systematic errors, while errors in X_{CO} ~~like SIF~~ are dominated by measurement noise.

1 Introduction

Carbon dioxide (CO₂) is the dominant anthropologically produced greenhouse gas (GHG) in the atmosphere. Its rapid increase in the last 170 years, due primarily from the use of fossil fuels, is changing the Earth's radiation budget leading to an increase in the mean temperature of the Earth's surface and resulting in ~~significant~~-secondary changes to the Earth's climate

5 ~~(Intergovernmental Panel on Climate Change (IPCC), 2013)~~including changes in weather and surface processes (Intergovernmental Panel on Climate Change (IPCC), 2013). Methane (CH₄) is the second most important anthropologically produced GHG with several sources including ~~oil~~ and gas mining, agriculture, coal mines, and municipal waste~~(?)~~. Finally, measuring carbon monoxide (CO) in the atmosphere is important for our understanding of tropospheric chemistry as a precursor to ozone (O₃), which is a pollutant in the troposphere ~~(Bergamaschi et al., 2000)~~(Granier et al., 1999; Bergamaschi et al., 2000), and is the primary sink for the hydroxyl radical (OH) (Crutzen, 1973; Logan et al., 1981), the concentration of which is important in estimating the oxidizing capacity of the atmosphere and ultimately the ability of the atmosphere to remove CH₄. Anthropogenic ~~Sources~~sources of CO include fossil fuel combustion and biomass burning (Kanakidou and Crutzen, 1999).

It is vital to make measurements of these gases, on ~~a~~-spatial and temporal ~~scale~~resolutions accurate enough to resolve sources and sinks, whether natural or anthropogenic ~~(Rayner and O'Brien, 2001; Miller et al., 2007; Shindell et al., 2006)~~(Rayner and O'Brien, 2001; Miller et al., 2007; Shindell et al., 2006). These measurements are then used in GHG flux inversion models ~~(?)~~(Bergamaschi et al., 2009; Crowell et al., 2018; Nassar et al., 2017; Sarrat et al., 2018) to improve our understanding of ~~the~~-GHG fluxes between the atmosphere and surface and, ultimately, in Earth system models, to understand the many complex climate feed-backs that lead to climate change (Sellers et al., 2018). Accurate measurements can be made from ground based networks (Wunch et al., 2011a, 2017) but these surface based measurements ~~are not made on spatial scales sufficient enough to constrain top-down flux inversions when compared to bottom-up inventories at point sources~~ (Gurney et al., 2003; ?)lack sufficient global coverage to estimate sources and sinks for all regions of the globe, especially in the poorly-sampled tropics (Gurney et al., 2003). Measurements of GHG concentrations from space have been shown to help fill this gap and provide measurements on spatial scales that can resolve sources and sinks, therefore reducing uncertainty in climate model predictions ~~(?)~~(Hakkarainen et al., 2016; Jacob et al., 2016; Buchwitz et al., 2017).

In the last few decades many satellite based missions dedicated to measuring greenhouse gas concentrations have been 25 successfully implemented, almost all of which are still currently acquiring data, and there are several that are planned for the future. The common objective of these missions is to measure the ~~dry-air-column-integrated-concentrations~~column-integrated dry-air mole fractions of CO₂, CH₄, and/or CO identified as ~~X_{CO₂}, X_{CH₄}, and X_{CO}~~X_{CO₂}, X_{CH₄}, and X_{CO}, respectively, with the goal of resolving sources and sinks of these gases. The Atmospheric Infra-Red Sounder (AIRS) is one of the first sensors that demonstrated the ability to measure CO₂ concentration (Chevallier et al., 2005) and the Measurement of Pollution in the Troposphere (MOPITT) instrument was the first instrument to demonstrate the ability to measure CO (Deeter et al., 2003; Edwards et al., 2004) in the atmosphere with the NIR.

It turns out that there is more signal ~~relative to greenhouse gas concentrations~~to make measurements to estimate greenhouse gas surface fluxes in the near-infrared (NIR) ~~(O'Brien et al., 1998; O'Brien and Rayner, 2002)~~ when observed at a high spectral resolution in the so-called "weak" CO₂ band at 1.61 μm and the "strong" CO₂ band at 2.1 μm~~, and, combined.~~ Combined

with the 0.76 μm O₂ A-band, the three bands provide sensitivity to other atmospheric characteristics, including surface pressure, temperature, aerosols and clouds, and the surface, that must be resolved to retrieve X_{gas} at the accuracy required to ~~make climate change predictions. The Measurement of Pollution in the Troposphere (MOPITT) instrument was the first instrument to demonstrate the ability to measure of CO (Deeter et al., 2004; Edwards et al., 2004) in the atmosphere with the NIR. Subsequently, there constrain sources and sinks. There~~ have been many successfully implemented polar orbiting missions, ~~lead-led~~ by countries across the world, that are partially or completely dedicated to measuring greenhouse gases by using hyperspectral measurements in these bands. These include SCIAMACHY (Bovensmann et al., 1999) ~~and TROPOMI (Veefkind et al., 2012): TROPOMI (Veefkind et al., 2012);~~ GOSAT (Kuze et al., 2009) and GOSAT-2 (~~Nakajima et al., 2012)~~ (Suto et al., 2021), using a Fourier transform spectrometer; and OCO-2 (Crisp et al., 2004) and OCO-3 (Eldering et al., 2019), with very similar measurement spectra compared to the GOSAT's but using a grating spectrometer. Finally, TanSat (Yang et al., 2018) is similar in design to the OCOs. Future missions include the third of the GOSAT series GOSAT-GW (Matsunaga and Tanimoto, 2022), Microcarb (Pascal et al., 2017), Sentinel-5/UVNS (Irizar et al., 2019), and the very ambitious constellation pair of satellites for CO₂M (Sierk et al., 2021). All of these missions vary in spatial coverage, spatial resolution, and spectral resolution. The one attribute that they have in common is that they are all on polar orbiting platforms which unfortunately limits their temporal resolution.

In addition, the 0.76 μm O₂ A-band measurements made by these instruments include Fraunhofer lines from which Solar-Induced Fluorescence (SIF) can be retrieved ~~Frankenberg et al. (2014); Somkuti et al. (2021) which has been shown to be Joiner et al. (2012); Frankenberg et al. (2014); Somkuti et al. (2021) which is~~ proportional to the photosynthetic activity of vegetation while considering several other factors including vegetation type and temporal variations(?). Subsequently, the rate of photosynthesis affects the rate of the uptake of CO₂(?). These measurements of SIF can then be used to improve carbon flux inversion model results.

The planned Geostationary Carbon Cycle Observatory (GeoCarb) differs from the polar orbiting missions in that it is in a geostationary orbit centered over the American continents (Moore III et al., 2018). ~~The mission is This approach has also been proposed before (Xi et al., 2015). The GeoCarb mission was~~ a collaboration between the USA's NASA and the Lockheed Martin Advanced Technology Center (LMATC). In a geostationary configuration GeoCarb will have the temporal resolution to resolve carbon cycle characteristics ~~unlike that capable that can be more difficult~~ with polar orbiters. The mission concept has been investigated including an initial investigation of the projected performance (Polonsky et al., 2014), a study of polarization dependence (O'Brien et al., 2015), and finally, an investigation of the ability of a geostationary mission ~~such~~-like GeoCarb to resolve greenhouse gas emissions on a shorter temporal scale (O'Brien et al., 2016; Rayner et al., 2002).

Of course radiometric measurements need to be converted to measurements of the physical quantities of interest using a ~~forward model inversion retrieval algorithm which is essentially the inversion of a forward model~~. In this case, ~~column-integrated greenhouse gas concentrations (X_{gas})~~ column-integrated dry-air mole fractions (X_{gas}) are the ~~so-called level-2 L2~~ products of use to the wider scientific community. In almost all the missions described above a form of an Optimal Estimation (OE) based algorithm for use in atmospheric retrievals is used, the application of which was ~~originally presented by Rodgers (1976, 1998) and formally presented by the same author in a treatise (Rodgers, 2004) Rodgers (2004) although some of these inversions~~

employ alternative approaches. Most of these methods are identified as so-called full-physics approaches in which the forward model approximates the physics as closely as practicably possible. The methods for these problems include linear methods such as the Weighting Function Modified Differential Optical Absorption Spectroscopy approach (WFM_DOAS) (Buchwitz et al., 2000) or nonlinear methods based on Newtonian iteration with some form of numerical regularization (Doicu et al., 2010).

5 WFM_DOAS has been shown to be viable for SCIAMACHY, TROPOMI, GOSAT, and OCO-2 measurements for all three gasses of interest (Buchwitz et al., 2005, 2006, 2017) and in a modified form with Full Spectral Initiation (FSI) to deal with pressure and temperature dependence of absorption lines (Frankenberg et al., 2005; Barkley et al., 2006). Other modifications algorithms have been presented to deal with the photon path length extension by aerosols (Bril et al., 2007; Butz et al., 2009) and to deal with the computational burdens of accounting for these aerosols (Reuter et al., 2017). Non-linear Nonlinear approaches,

10 although more computationally intensive, are being used for the same selection of instruments (Buchwitz et al., 2017) in order to obtain as much information as possible in what is a largely an unconstrained optimal inversion. This is especially true in the case of resolving aerosol/cloud properties (Reuter et al., 2010). There are several OE algorithms for the retrieval of ~~X_{CO_2}~~ , ~~X_{CH_4}~~ , ~~X_{CO}~~ , and/or ~~X_{CO}~~ applied to measurements from many instruments including AIRS (Chevallier et al., 2005), with measurements in the IR, or in the NIR: SCIAMACHY (Butz et al., 2010), TROPOMI (Hu et al., 2016; Landgraf et al., 2016), ~~the~~ GOSAT-1/2 (Yokota et al., 2009; Yoshida et al., 2011), and OCO-2/3 (Connor et al., 2008; O'Dell et al., 2012; Crisp et al., 2012; O'Dell et al., 2018). In some cases, due to the convenient generality of OE, the algorithms can be applied to a number of instruments, including the use of the Atmospheric Concentrations from Space (ACOS) algorithm (?). For GeoCarb the plan is to use the L2 (O'Dell et al., 2012; Crisp et al., 2012) and the RemoTeC algorithm (Butz et al., 2009, 2010). As first proposed in Polonsky et al. (2014), for GeoCarb we use the heritage from the ACOS retrieval algorithm; currently used for

20 OCO-2, OCO-3, and GOSAT L2 ~~product to simultaneously to retrieve X_{CO_2} , X_{CH_4} products; to simultaneously retrieve X_{CO_2} , X_{CH_4}~~ , and/or ~~X_{CO}~~ from GeoCarb measurements.

In this paper we formally present the GeoCarb level-2 (L2) optimal estimation OE algorithm and build on previous research with simulation experiments to determine the sensitivity to several sources of uncertainty an error budget for each target gas. SIF measurements from GeoCarb have been been previous discussed in Somkuti et al. (2021) and are not further discussed here unless otherwise noted. In section 2 the GeoCarb mission is discussed including its orbital configuration, the instrument characteristics, and the current challenges faced. Section 3 discusses the details of the GeoCarb L2 retrieval algorithm including the inversion methodology, forward model, state vector, and both pre- and post-processing. Section 4 describes the analysis setup including the scan strategy used, the details of the measurement data simulations, and the details of the individual perturbation experiments. In section 5 the results of the perturbation experiments are presented along with an error budget

25 table derived from the results. Finally, in section 6, some concluding remarks are given including some points to take away from the research, and an outlook of future work.

It is important to note that this study has similarities with Polonsky et al. (2014) and O'Brien et al. (2015), hereafter referred to as P2014 and O2015, respectively. These similarities include that the same four bands are used. The same three gasses are retrieved (CO_2 , CH_4 , and CO). The simulation of synthetic radiances is performed with effectively the same code base. Finally, our meteorology and polarization tests are similar to that performed in P2014 and O2015, respectively.

Differences with P2014 and O2015 include that there are theoretical instrument model updates that reflect the current design vs. that used in P2014 and O2015 including the radiometric calibration, instrument line shape, and polarization. Our L2FP algorithm builds off of a more recent version of the ACOS L2FP algorithm. The previous publications simulate whole global, polar orbits. We use a real geostationary observation strategy similar to that envisioned for GeoCarb. The previous publications discuss “descope” options in terms of using less bands. We do not, as these were no longer considered at the time. We retrieved profiles of CH₄ and CO concentrations rather than profile scaling factors and calculated averaging kernels for these gases from those profile retrievals. P2014 and O2015 did not test sensitivities to any instrument errors. We test sensitivities to radiometric calibration, instrument line shape, polarization, and pointing. Although, as noted later, there are other instrument errors that are left for future studies. Finally, We include sensitivity to spectroscopic errors such as that explored by Connor et al. (2016) for OCO-2 in the context of X_{CO₂} retrievals.

Finally, it is also important to note that the GeoCarb mission was cancelled by NASA, although, the instrument is still in development and will be delivered to NASA, in full, with the hope that it will eventually be adopted in a future mission proposal.

2 GeoCarb mission and instrument

~~The Geostationary Carbon Cycle Observatory (GeoCarb)~~ GeoCarb (Moore III et al., 2018) was selected as the NASA’s second Earth Venture ~~Mission-2~~ Mission (EVM-2). The scientific objectives of GeoCarb are to ~~advanced~~ advance our knowledge of the carbon cycle, in particular land-atmosphere fluxes of carbon dioxide (CO₂) and methane (CH₄). This requires measurements of ~~total atmosphere column amounts~~ column-integrated dry-air mole fractions of CO₂, CH₄, and ~~carbon monoxide (CO)~~ CO, in addition to ~~solar induced fluorescence (SIF)~~ SIF, at urban to continental scales and at spatial and temporal resolutions that are sufficient enough to significantly improve land-atmosphere CO₂ and CH₄ flux estimates and reduce the uncertainty of these fluxes.

To meet ~~the scientific objectives~~ scientific objectives, the GeoCarb mission ~~will develop~~ is developing a multi-band, hyperspectral, Littrow Grating Mapping Spectrometer (GMS) which will be hosted on a ~~telecommunications~~ satellite in a geostationary orbit with a sub-satellite point (SSP) that is currently set to be 103° west longitude, although the SSP may change when the host platform is finalized. GeoCarb will measure reflected ~~sun light~~ sunlight in four absorption bands and retrieve ~~atmospheric column concentrations~~ column-integrated dry-air mole fractions of CO₂, CH₄, and CO known as X_{CO₂}, X_{CH₄}, and X_{CO}, respectively, defined by

$$X_{\text{gas}} = \frac{\int_0^{\infty} u_{\text{gas}}(z) N_d(z) dz}{\int_0^{\infty} N_d(z) dz}, \quad (1)$$

where $u_{\text{gas}}(z)$ is the gas mole fraction with respect to dry air at altitude z and $N_d(z)$ is the total molecular number density of dry air at altitude z . The relative and absolute mission ~~accuracy-precision~~ requirements for X_{gas} are listed in table 1. These requirements are specifically for multi-sounding precision on at least 100 aerosol-cloud-free (vertically-integrated AOT + COT

< 0.3), as determined against colocated Total Carbon Column Observing Network (TCCON) observations (Wunch et al., 2017)

Table 1. GeoCarb ~~mission-multi-sounding~~ precision requirements for the ~~main-three-primary~~ target trace gases.

Gas	Relative	Absolute
X_{CO_2}	0.3 %	1.2 ppm
X_{CH_4}	0.6 %	10 ppb
X_{CO}	10 %	12 ppb

The four GeoCarb bands, listed in table ??-2 and plotted in figure 1, include the O₂ A-band at 0.765 μm, the weak CO₂ band at 1.606 μm, the strong CO₂ band at 2.065 μm, and a CH₄/CO band at 2.323 μm (referred to as the CH₄ band hereafter). The four bands have spectral resolutions Δλ, defined as the full width at half maximum (FWHM) of the instrument line shape (ILS), of 0.044 nm, 0.091 nm, 0.114 nm, and 0.129 nm with resolving powers (λ/δλ) of ~~17366, 17661, 18120, and 18012~~ roughly 17400, 17600, 18100, and 18000, respectively. The required signal-to-noise ratios (SNR) are listed in table ??-2 for each band along with the relative reference radiance levels. The O₂ A-band provides information on surface pressure, clouds and aerosols. In addition, the O₂ A-band includes Fraunhofer lines from which SIF can be retrieved. The weak CO₂ band and the strong CO₂ band provide information on column CO₂ ~~concentrations-fractions~~ and clouds and aerosols while the strong CO₂ band also provides information on H₂O concentration. These first ~~3-bands-are-quite~~ ~~three bands are~~ similar in spectral range and resolution to those on ~~the Orbital Carbon Observatories-OCO-2 and OCO-3~~. The fourth band adds the ability to retrieve CH₄ and CO₂ and also provides information on H₂O and hydrogen-deuterium oxide (HDO).

20 **GeoCarb signal-to-noise ratio (SNR) for each of the four bands:**

The current set of satellite missions capable of measuring atmospheric greenhouse gas concentrations, including OCO-2, OCO-3, ~~the Greenhouse Gases Observing Satellites (GOSAT) 1 and 2 and the TROPOspheric Monitoring Instrument (TROPOMI)~~ ~~GOSAT-1, GOSAT-2, and TROPOMI~~ are all in polar orbits that cover most or all of the Earth's surface but only with a limited temporal sampling. GeoCarb ~~is-was~~ the first planned ~~geostationary-geostationary~~ Earth observation mission for

Table 2. GeoCarb spectrometer parameters as stated in the mission requirements.

Band Number	Band Name	Band wavelength (μm)	Spectral Range (nm)	Channel spacing (nm)	Spectral Resolution Δλ (nm)	SNR	Reference radiance (W/m ² /sr/μm)
1	O ₂ -A	0.765	756.5 – 771.7	0.015	0.044	395	71
2	CO ₂ , weak	1.606	1591.5 – 1622.8	0.031	0.091	389	14
3	CO ₂ , strong	2.065	2044.3 – 2087.1	0.042	0.114	302	5.0
4	CH ₄	2.323	2299.3 – 2347.8	0.048	0.129	254	2.7

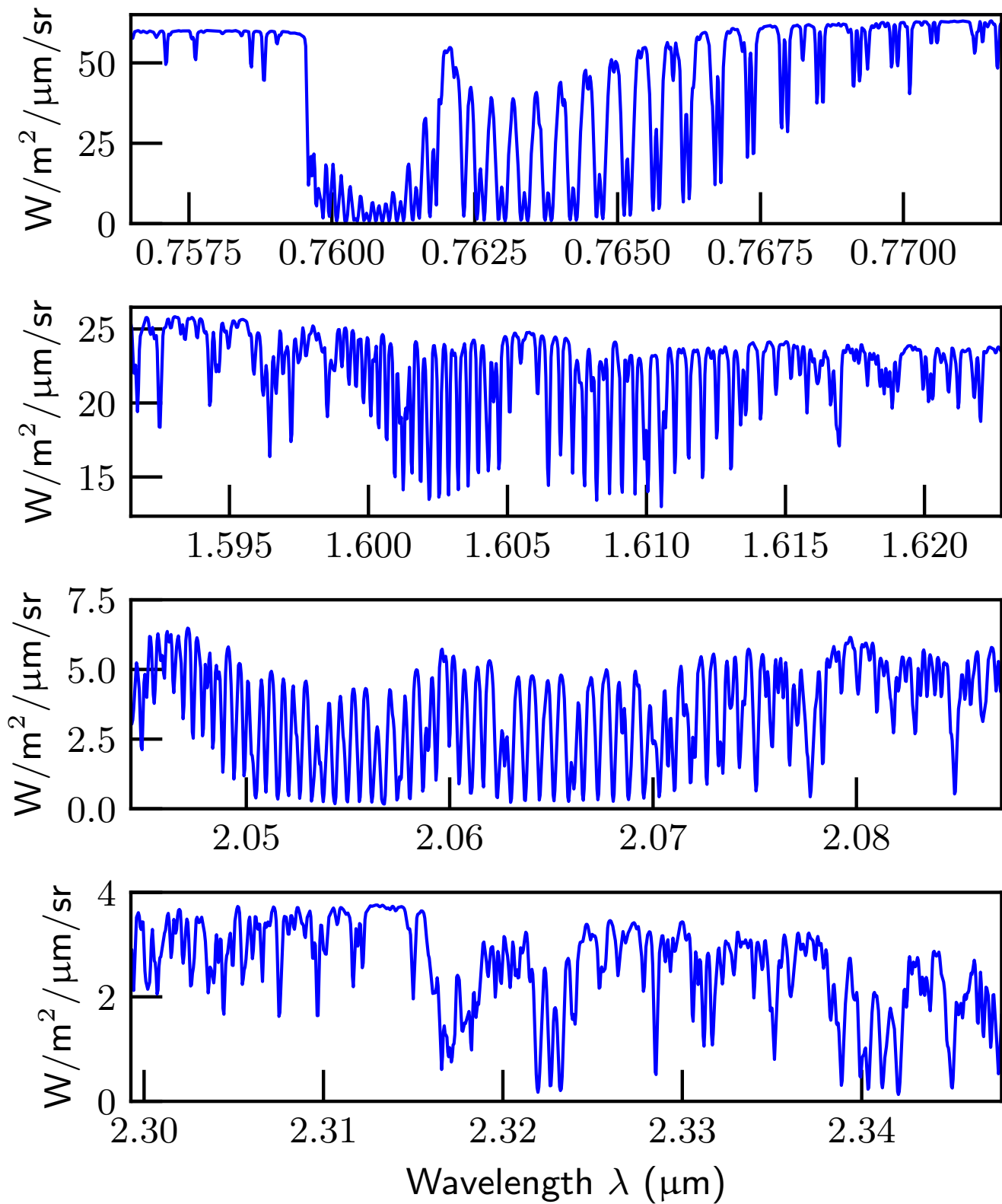


Figure 1. Sample spectrums of observed radiance from a typical airmass scenario. Panels include, from top to bottom, the O₂ A, weak CO₂, strong CO₂, and CH₄ bands, respectively.

25 measuring greenhouse gases and SIF, distinguishing it from the ~~polar-orbiting-current suite of polar orbiting GHG~~ missions. In a geosynchronous orbit, with its configurable imaging/mapping capability, it will be able to measure X_{CO_2} , X_{CH_4} , and X_{CO} at the urban to continental scales and at the spatial and temporal resolutions that are sufficient enough to resolve emission sources and significantly improve land-atmosphere CO_2 and CH_4 flux calculations and reduce the uncertainty of these fluxes. ~~In a geosynchronous orbit the entire Earth disk is visible, centered at the SSP and unlike a polar orbiter~~ Hence, GeoCarb is
5 capable of acquiring multiple observations of the same location per day for most of the Western Hemisphere. Since GeoCarb is not configured to make ocean glint observations regularly, retrievals over ocean will not be made operationally.

~~The GeoCarb "scan strategy"~~ The GeoCarb scan strategy will include a set of scan blocks that cover most of the land ~~surface~~ surface surfaces of North, South, and Central America, up to three times a day. The scan strategy will minimize overlap between blocks and observations over ocean and will be optimized for SNR-signal-to-noise ratio (SNR) with respect to solar zenith angle and
10 airmass factor. The scan blocks are configurable in location, size, and frequency. This allows GeoCarb to alter its scan strategy to intensively scan smaller regions of particular interest or uncertainty many times a day, for detailed emission estimates, for calibration and validation, or for transient events in a campaign mode. The scan strategy has yet to be formalized, although proposed strategies have been published in the literature (Nivitanont et al., 2019b; Somkuti et al., 2021).

GeoCarb is equipped with ~~two grating spectrometers that measure incoming reflected sunlight. One spectrometer a four-band~~
15 spectrometer with two arms. The short-wave (SW) arm covers the O_2 A-band ($0.765 \mu\text{m}$) and the weak CO_2 band ($1.606 \mu\text{m}$) ~~and the other spectrometer, and the long-wave (LW) arm~~ covers the strong CO_2 band ($2.065 \mu\text{m}$) and the CH_4/CO band ($2.323 \mu\text{m}$). Light is first incident on two orthogonally oriented scan mirrors used for pointing. This light is then transmitted to ~~an~~ an
~~off-axis-parabolic-afocal-a three mirror anastigmat~~ telescope with a ~~72-54~~ mm entrance aperture and ~~4.4°-a 4.3°~~ field-of-view (FOV) ~~which produces a collimated beam that is directed toward a dichroic beam splitter separating SW and LW for each~~
20 ~~spectrometer followed by an objective lens group for each path that forms,~~ forming a well-corrected image on an $18 \text{ mm} \times 0.036$ ~~0.042~~ mm spectrometer entrance slit. ~~Each spectrometer has a single grating from the which the two bands per grating are separated into orders and selected by narrow band order sorting filters illuminating one of two~~ Following the slit, a dichroic beamsplitter separates the SW and LW channels to the two arms of the spectrometer, each with a single echelle grating used in two orders. Additional dichroic beamsplitters direct the light to one of the focal plane assemblies (FPAs) specific to each
25 band ~~, so that there are a total of four FPAs used in the instrument with a narrowband order sorter filter ahead of the FPAs.~~ The FPAs are ~~of size HgCdTe detectors with 1016 in the spatial dimension \times 1016 in the spectral dimension. The optical alignment is such that the spatial dimension is along the slit and the spectral dimension is across the slit~~ active pixels, with the spatial direction along columns and the dispersion direction along rows.

The slit is projected on the Earth with the spatial dimension oriented north-south (N-S). The angular size of the slit is ~~4.4°~~
30 4.3° in the along-slit direction and 0.00833° in the across-slit direction. At the SSP, this is 25° in latitude or 2800 km N-S on the surface of the Earth. Given the $18 \text{ mm} \times 0.036$ ~~0.042~~ mm size of the slit and the 1016 samples of the FPA distributed along-slit, the angular resolution for a single footprint is approximately $123 \mu\text{rad}$ along-slit at nadir. At the geostationary altitude of 35786 km this results in a footprint size of approximately 2.7 km along-slit (at the slit center, increasing by 2.4% toward the slit ends because of Earth curvature) and 5.4 km across-slit at nadir. The slit is pointed utilizing the two orthogonally oriented

35 scan mirrors, a N–S scan mirror that can be rotated a total of $\pm 3.55^\circ$ and an E–W scan mirror that can be rotated a total of $\pm 5.00^\circ$. These mirrors are capable of pointing the slit over a range of 20° in the N–S direction and 18.5° in the E–W direction, respectively, which covers the Earth disc with a diameter of 17.4° viewed from the geostationary orbit. For each scan block the E–W scan mirror will move in equiangular steps in a step-and-stare mode with 0.3825 s per step and 9.0 s per stare (integration time). The E–W scan rate is $2.7 \text{ km} / 4.4625 \text{ s} = 2178 \text{ km/h}$ so that continental width scans are completed in 1.5 to 3 hours.

5 ~~Several optical aberrations that occur in the GeoCarb optics are under investigation to understand their effects and to develop rectification methods for the effects in either the measured radiances or in the retrievals. The aberrations include “smile”, the “keystone effect”, “stray light”, “detector persistence”, and ultimately effects related to scene inhomogeneity. Smile is an effect caused by a change in dispersion over the FOV so that the spectra measured at the middle of the FOV is increasingly offset spectrally from that measured towards the sides. The keystone effect is a spatial misregistration of the spectrum that involves~~
10 ~~the sensors ability to measure the spectra from a single point without being influenced by surrounding points, i.e. without mixing spectra from adjacent positions in the FOV. Stray light is any light reaching a detector that is outside the wavelength range of the detector. It comes from imperfections in the instrument optics and subsequently may be scattered off the rest of the instrument hardware into the detectors. Detector persistence occurs when the signal from a particular scene on a detector persists long enough to be prevalent when observing a following scene. The persistent signal decays exponentially with time and is particularly important when observing a bright scene followed by a dark scene.~~

15 Due to GeoCarb’s step-and-stare scanning method and high spectral resolution, the instrument is sensitive to across-slit scene inhomogeneity. In the context of greenhouse gas measurements, this has been discussed by several authors (Landgraf et al., 2016; Meister et al., 2017; Nivitanont et al., 2019a). In particular, the effective instrument ILS will vary across an FOV depending on the scene brightness inhomogeneity within the FOV. One method of mitigating this effect is by installing
20 a slit-homogenizer into the optical assembly effectively smearing out the inhomogeneity across the FOV. Due to schedule constraints during instrument assembly, the decision was made to remove the homogenizer and replace it with an airlit. Another mitigation method, and currently planned for GeoCarb, is to fit for an ILS “stretch” scaling factor for each band in the L2 retrieval, effectively scaling the full-width-at-half-maximum (FWHM)FWHM, which will either stretch or squash the ILS making it broader or narrower, therefore optimizing the ILS for each FOV.

25 There are several other instrument related uncertainties that occur in the GeoCarb instrument that are under investigation to understand their effects and to develop rectification methods for those effects in either the measured radiances or in the retrievals. These include “smile”, the “keystone effect”, “stray light”, “detector persistence”, and ultimately effects related to scene inhomogeneity.

30 Calibrated, spectrally resolved radiances for each of the four bands will be distributed in level-1B (L1B) files which also contain the measurement’s geolocation, solar and satellite geometry, instrument characteristics, and other parameters normally required to make use of the measurements. In addition, each L1B file will be distributed with a “Met” file that contains meteorological information required for the level-2 (L2)-retrievalretrievals.

3 Level-2 retrieval algorithm

The GeoCarb [Level-2 \(L2 \)](#)-retrieval algorithm code, also known as L2 full-physics (L2FP), is a fork of the L2FP code developed at the NASA Jet Propulsion Laboratory (JPL) since 2004 for OCO and then subsequently for GOSAT (2009), OCO-2 (2014), and OCO-3 (2019) (Connor et al., 2008; O’Dell et al., 2012; Crisp et al., 2012; O’Dell et al., 2018). Development of the GeoCarb fork maintains backward compatibility with the OCO-2/3 base which means that not only can it be used for the same instruments as the JPL code base but also that improvements made to the JPL code are merged into the GeoCarb code base. In this section [a brief an](#) overview of the retrieval algorithm is given with focus on changes made to the GeoCarb code base relative to the OCO-2/3 code base in detail.

3.1 Inversion

The inversion methodology used in the GeoCarb L2FP retrieval is based on the [optimal-estimation OE](#) approach for atmospheric inverse problems described by Rodgers (2004) in which input parameters to a *forward model* are optimized to obtain the best match between real measurements and simulated measurements output from a forward model while being constrained by a priori knowledge of the input parameters. This relationship is given by

$$\mathbf{y} = \mathbf{F}(\mathbf{x}, \mathbf{b}) + \epsilon, \quad (2)$$

where \mathbf{F} is the forward model, \mathbf{x} is the n element input state vector containing the input parameters to be optimized, \mathbf{y} is the m element measurement vector containing the calibrated radiance spectra for all [4-four](#) bands ($m = 4 \times 1016$), \mathbf{b} is the set of all other assumed model parameters not in the state vector \mathbf{x} , and ϵ represents the measurement and forward model error. The inverse solution for the optimized state vector $\hat{\mathbf{x}}$ is obtained by minimizing a cost function which can be expressed as a χ^2 distribution given by

$$\chi^2 = [\mathbf{y} - \mathbf{F}(\mathbf{x}, \mathbf{b})]^T \mathbf{S}_\epsilon^{-1} [\mathbf{y} - \mathbf{F}(\mathbf{x}, \mathbf{b})] + (\mathbf{x} - \mathbf{x}_a)^T \mathbf{S}_a^{-1} (\mathbf{x} - \mathbf{x}_a), \quad (3)$$

where \mathbf{S}_ϵ is the measurement and forward model error covariance matrix, \mathbf{x}_a is the *a priori* state vector and \mathbf{S}_a is the *a priori* error covariance matrix. \mathbf{x}_a and \mathbf{S}_a denote the best guess of the state before the measurement is made and the uncertainty of this guess, respectively.

[The retrieval problem is ill-posed leading to non-existence, non-uniqueness \(due to discretization of the problem\) and/or ill-conditioning \(due to amplification of errors in \$\mathbf{x}\$ due to errors in \$\mathbf{y}\$ \). It is for this reason that an a priori constraint is required. The fact that the problem is nonlinear requires an iterative method. Finally, in order to perform the iteration efficiently, while maintaining a stable step size, a form of regularization is required. To satisfy these requirements the Levenberg-Marquardt \(Levenberg, 1944; Marquardt, 1963\) method is applied to Gauss-Newton iteration \(Rodgers, 2004; Connor et al., 2008\).](#)

[After successful convergence an estimate of the a posteriori covariance matrix \$\hat{\mathbf{S}}\$ is computed. Several other information and diagnostic quantities are also produced and included in the L2FP product including the averaging kernel matrix \$\mathbf{A}\$ and the number of degrees of freedom for signal \$d_s\$. See Connor et al. \(2008\) for a full description of the quantities.](#)

3.2 Forward model

The forward model $\mathbf{y} = \mathbf{F}(\mathbf{x}, \mathbf{b})$ takes as input the state vector \mathbf{x} , containing the parameters to be optimized, and the vector of assumed parameters \mathbf{b} that are not optimized and simulates the measurements observed by the GeoCarb instrument, i.e. the radiances observed in the 1016 channels in each of the 4 bands. The forward model also computes (analytically) the derivatives of the measurements simulates the measurements in \mathbf{y} and analytically computes the derivatives in the matrix \mathbf{K} with respect to the state vector parameters which are contained in the Jacobian matrix \mathbf{K} required for the inversion iteration.

Most of the current forward model has been described in detail by O'Dell et al. (2012) and (O'Dell et al., 2018) O'Dell et al. (2018) in the context of the OCO-2 mission and is only described briefly in this section. However, there are some instrument model changes specific to GeoCarb which includes include noise, polarization, and the ILS.

The forward model can be broken down into several sub-models: an atmospheric model, surface model, instrument model, a gas absorption model, an aerosol model, a surface model, a solar model, and a radiative transfer (RT) model, and finally an instrument model. The atmospheric model discretizes the atmosphere into a 20 layers using a sigma-pressure level system where the pressure levels scale with surface pressure and the top most level is at 0.01 hPa. Parameters including temperature and humidity, trace gas concentrations, and aerosol/cloud concentrations are defined on each level by their various models from which the wavelength dependent layer quantities required for the RT computations are computed along with a layer at the bottom for the atmosphere for surface reflectance. All but the instrument model are explained in detail in the references cited and will not be reiterated here. Here we will focus on the instrument model in the context of GeoCarb.

3.2.1 Instrument model

The instrument model consists of three components: 1) a polarimetric model, 2) an instrument line shape (ILS), and 3) a noise model which are described below. Note that the optical aberrations other instrument effects discussed in section 2 are not accounted for in the instrument model presented and therefore are ignored in this study.

3.2.1.1 Polarimetric model

The polarimetric model predicts the intensity that is eventually incident on the detectors after being transmitted through the scan mirrors, telescope, beam splitter, and gratings. The polarization effects of each of the optical components can be linearly combined into a single wavelength dependent Muller matrix (O'Brien et al., 2015) as shown in O2015. The intensity is computed with a simple matrix transformation on the Stokes vector $\mathbf{S}(\lambda) = [I(\lambda), Q(\lambda), U(\lambda), V(\lambda)]$ incident on the scan mirrors by the 4×4 Muller matrix $\mathbf{M}(\lambda)$ for which the wavelength dependence is linear across each band:

$$I_{b,i} = \mathbf{M}_{b,0} \mathbf{S}_{b,i} + \mathbf{M}_{b,1} \mathbf{S}_{b,i} (\lambda_i - \lambda_0), \quad (4)$$

where $I_{b,i}$ is the radiance for band b , at the high resolution grid point i ; $\mathbf{M}_{b,j}$ is the 1×4 Mueller matrix for band b and linear dependence order $j = 0, 1$; and $\mathbf{S}(\lambda) \mathbf{S}_{b,i}$ is the Stokes vector. The four elements of the Mueller matrix, often called the Stokes coefficients, are $m_{00,b,j}, m_{01,b,j}, m_{02,b,j}, m_{03,b,j}$ and are determined during pre-flight polarimetric calibration. It

should be noted the last element of the Stokes vector is typically small as the surface and atmosphere generate very little circular polarization, therefore, to save processing time, the RT is computed using only the first three elements of the Stokes vector and a 1×3 Mueller matrix. Finally, we note that for GeoCarb, equation 4 can be written in a simplified form as:

$$I_{b,i} = I(\lambda_i) + [c_0 + c_1(\lambda_i - \lambda_0)] \times (Q(\lambda_i) \cos 2\phi_p - U(\lambda_i) \sin 2\phi_p), \quad (5)$$

where c_0 and c_1 are primarily functions of the grating efficiency as a function of wavelength in each band, and ϕ_p represents the angle between the axis of vertical polarization (with respect to the grating) and the reference plane for polarization. Both Stokes components Q and U also depend upon the chosen reference plane for polarization. We follow the OCO-2/3 convention and choose the local meridian plane to be this reference plane for polarization, which is the plane containing the local normal unit vector and the vector pointing from the target FOV to the satellite. For further details, see O2015.

3.2.1.2 ILS Convolution

The radiance measured in each of the 1016 spectral channels, of each of the 4-four bands, for each of the 1016 footprints along the slit, is the result of the convolution of intensity computed on a high spectral resolution ($0.01 \mu\text{m}$) spectral grid with a instrument spectral response function:

$$I_{f,b,c} = \int_{\lambda_0}^{\infty} I_{f,b,i} \text{ILS}_{f,b,c}(\lambda) d\lambda, \quad (6)$$

where $I_{f,b,c}$ is the radiance for footprint f , band b , and channel c ; $I_{f,b,i}$ is the radiance for footprint f , band b , and high resolution grid point i ; and $\text{ILS}_{f,b,c}(\lambda)$ is the, footprint, band, and channel dependent ILS as a function of wavelength λ . In practice, the integration is performed over a limited range centered on each channel of 0.00082 , 0.0022 , 0.0028 , and $0.0025 \mu\text{m}$ for bands 1, 2, 3, and 4 respectively.

3.2.1.3 Radiometric noise model

The instrument noise model is used to build the measurement and forward model error covariance matrix \mathbf{S}_ϵ . In addition, for the retrieval simulation experiments presented in section 4, the noise model is used to add synthetic noise to the simulated measurements. The noise model ~~for GeoCarb is based on both laboratory characterization and airborne trials with the Tropospheric Mapping Imaging Spectrometer (TIMS) developed by Lockheed Martin (Kumer et al., 2009, 2011) and is described in detail by Kumer et al. (2013)~~ will ultimately be based on laboratory measurements although for this study the model (of the same form) is based on theory but we expect that the outcome of the experiments presented will not change significantly with final noise model based on measurements. The standard deviation of noise $\sigma_{I_{b,c}}$ for band b and channel c is given by

$$\sigma_{I_{b,c}} = \sqrt{n_{0,b,c}^2 + n_{1,b,c} I_{b,c}}, \quad (7)$$

Table 3. GeoCarb noise coefficients used in this study, in units of $\text{W m}^{-2} \text{sr}^{-1} \mu\text{m}^{-1}$

<u>Band</u>	<u>n_0</u>	<u>n_1</u>
<u>1</u>	<u>2.291e-2</u>	<u>1.953e-4</u>
<u>2</u>	<u>5.023e-3</u>	<u>4.282e-5</u>
<u>3</u>	<u>3.224e-3</u>	<u>2.646e-5</u>
<u>4</u>	<u>3.472e-3</u>	<u>2.094e-5</u>

where $n_{0,b,c}^2$ is the background noise coefficient, $n_{1,b,c}$ is the coefficient for noise proportional to the radiance (shot noise) $I_{b,c}$, and the radiance and the coefficients are in units of $\text{Wm}^{-2}\text{sr}^{-1}\mu\text{m}^{-1}$. Unlike the ILS, the instrument noise is independent of the footprint f along the slit, but does vary (roughly quadratically) with wavelength in each band. Table 3 gives the mean noise
 15 coefficients for each band used in this study. Like the other instrument parameters, noise coefficients will be determined during
preflight calibration.

3.3 State vector and a priori

The state vector \mathbf{x} contains the parameters that are optimized during the inversion process. The parameters include values that are used to compute the retrieval values of: X_{CO_2} , X_{CH_4} , and X_{CO} , in addition to other parameters that are sensitive to the
 20 measurements but are not known perfectly, such as meteorological, aerosol/cloud, surface, and instrument related parameters. Much of the state vector is described in detail by O’Dell et al. (2012) and (O’Dell et al., 2018). Here the state vector elements are discussed focusing in detail on elements added for GeoCarb. In total there are $n = 78$ fitted parameters in the state vector. The prior values used for these parameters are also described as are their associated error covariances. Table 4 presents the state vector along with the priors and associated 1σ uncertainties.

25 CO_2 is represented in the state vector as a profile of dry-air mole fraction on the forward model’s 20 sigma-pressure levels. CH_4 and CO profile retrievals are typically limited to $\approx 1 \sim 1$ degree of freedom for signal d_s so for GeoCarb a scaling retrieval is performed for these gases, where the prior profile is scaled by a single retrieved parameter with a prior value of unity. The prior CO_2 , CH_4 , and CO profiles are nearly identical to those used in the GGG2020 ~~Total Carbon Column Observing Network (TCCON)~~ TCCON retrieval Wunch et al. (2017) produced as described in ~~(?)~~ (Laughner et al., 2023). The CO_2 prior
 30 covariance matrix is constructed such that the total prior uncertainty of X_{CO_2} is 12 ppm, a value somewhat larger than natural variability, that gives more weight to the measurements relative to the prior. The prior uncertainties for the CH_4 and CO scale factors are both set to 0.5.

Meteorological quantities included in the state vector are surface pressure, a temperature profile offset, and a water vapor profile multiplier. Surface pressure is included to account for path length modification effects and other systematic errors common to the absorption bands used in the retrieval. The temperature and water vapor profiles both affect trace gas absorption while water vapor is in itself an important absorber across all four bands. The prior surface pressure and temperature and water vapor profiles are obtained from the Goddard Earth Observing System Data Assimilation System (GEOS-5) Forward

Table 4. GeoCarb state vector and a priori. ([See table 2 in O’Dell et al. \(2018\)](#) for a full description of the parameters and comparison to the [OCO-2/OCO-3 state vector.](#))

Parameter	Length	A priori	A priori uncertainty (1σ)	Notes
CO ₂ profile	20	GGG2020 TCCON	Fixed covariance matrix	Defined on σ pressure levels, mole fraction wrt dry air
CH ₄ scaling factor	1	1.0	0.5	Multiplier on prior profile from GGG2020 TCCON
CO scaling factor	1	1.0	0.5	Multiplier on prior profile from GGG2020 TCCON
Surface pressure	1	From GEOS-5	4.0 hPa	
Temperature offset	1	0 K	5 K	Added to prior profile
H ₂ O scaling factor	1	1.0	0.5	Multiplier on prior profile
Aerosol 1 OT _{0.755}	1	From GEOS-5	\pm factor of 7.39	
Aerosol 1 x_0	1	0.9	0.2	Units of relative pressure
Aerosol 1 σ_a	1	0.05	0.01	Units of relative pressure
Aerosol 2 OT _{0.755}	1	From GEOS-5	\pm factor of 7.39	
Aerosol 2 x_0	1	0.9	0.2	Units of relative pressure
Aerosol 2 σ_a	1	0.05	0.01	Units of relative pressure
Water cloud OT _{0.755}	1	0.0125	\pm factor of 6.05	
Water cloud x_0	1	0.75	0.4	Units of relative pressure
Water cloud σ_a	1	0.1	0.01	Units of relative pressure
Ice cloud OD _{0.755}	1	0.0125	\pm factor of 6.05	
Ice cloud x_0	1	Just below tropopause	0.2	Units of relative pressure
Ice cloud σ_a	1	0.04	0.01	Units of relative pressure
Strat. aerosol OD _{0.755}	1	0.006	1.8	
Strat. aerosol x_0	1	0.03	0.0001	Units of relative pressure
Strat. aerosol σ_a	1	0.04	0.01	Units of relative pressure
BRDF weight	1 per band	From band continuum	5.0	From the continuum level per band
BRDF weight slope	1 per band	0.0 1/cm ⁻¹	0.001 1/cm ⁻¹	
BRDF weight quadratic	1 per band	0.0 1/cm ⁻²	0.000005 1/cm ⁻²	
Dispersion offset	1 per band	From dispersion (μm)	0.4 of FWHM (μm)	Coef. 0 of dispersion polynomial
Dispersion scale	1 per band	From dispersion	0.000001	Coef. 1 of dispersion polynomial
ILS scale factor	1 per band	1.0	0.032	Multiplier on ILS $\Delta\lambda$
EOF amplitudes	3 per band	0.0	10.0	Multiplier on EOF spectral pattern
SIF mean	1	0.0	0.02	Not the official SIF retrieval
SIF slope	1	0.0018 1/cm ⁻¹	0.0000007 1/cm ⁻¹	Not the official SIF retrieval

Processing for Instrument Teams (FP-IT) forecast (Rienecker et al., 2008; Lucchesi, 2013). The prior uncertainties of surface
5 pressure, the temperature profile offset, and the water vapor scale are set to 4 hPa, 5 K and 0.5, respectively.

For particles two tropospheric aerosol types, liquid water cloud, ice cloud, and a stratospheric aerosol are included in the
state vector \mathbf{r} , ~~for each of which including their density x_0 , the 1σ profile width σ_a , and $\ln(\text{OT})$~~ the natural logarithm of the
optical thickness (OT) at $0.755 \mu\text{m}$ $\ln(\text{OT}_{0.755})$ are fitted for. ~~Five aerosol types are possible based on an aggregation of the 15~~
10 ~~aerosol types possible based on an aerosol climatology created from the Modern-Era Retrospective analysis for Research and~~
Applications (MERRA)(Rienecker et al., 2011). For each sounding the two tropospheric aerosol types with the highest mean
monthly values of the $\text{OT}_{0.755}$ ~~are retrieved. Optical properties are pre-computed for the aerosol types and optical properties~~
~~for liquid water cloud are for a Gamma distribution (Hansen, 1971) of spherical drops with an effective radius of $8 \mu\text{m}$ and for~~
~~ice cloud are taken from (Baum et al., 2014)~~ based on the MERRA climatology are chosen.

The surface BRDF amplitude weight, weight slope, and weight quadratic terms are included in the state vector for each
15 band. The prior weight values are estimated directly from the level of the continuum in the observed spectrum of each band,
assuming a clear-sky, absorption-free atmosphere, and prior slopes and quadratic parameters are set to zero. The corresponding
prior uncertainties are set to sufficiently large values so that the amplitude parameters are essentially unconstrained.

The dispersion scale and offset coefficients are included in the state vector for each band. The prior values are simply set to
~~coefficient~~ zero and one, respectively, of the dispersion polynomial for each band. The prior uncertainties for the offset are set
20 to $0.4 \times$ the FWHM for each band and for the scale are set to ~~0.000001~~ 10^{-6} for each band.

To mitigate the effects of the scene inhomogeneity on the ILS across the scene an ILS stretch scaling factor is fitted for each
band effectively scaling the FWHM ~~which will either stretch or squash the ILS making making it broader or narrower.~~ The
prior stretch scaling is set to unity with a prior uncertainty of 0.032 for each band.

Spectral residuals, the difference between the measured radiance and the modeled radiance from the retrieved state vector,
25 contain systematic structure due to unknown spectroscopic errors, solar model errors, and instrument characteristics. To account
for these residuals empirical orthogonal functions (EOFs) are created from a clear-sky training dataset to represent the spectral
patterns, for which, amplitude factors are included in the state vector and fitted for per band and per EOF. The prior amplitude
factors for each band are set to zero with prior uncertainties of 10.0 each.

To account for the effects of SIF emission from the vegetation on the surface two SIF parameters are fitted for: a mean and a
30 slope across the O_2 A-band. It is important to note that the SIF parameters in the state vector are not the official GeoCarb SIF
product which is produced by the Generic Algorithm for the Single Band Acquisition of Gases (GASBAG) briefly introduced
in section 3.5.2 and discussed in detail by Somkuti et al. (2021). The prior SIF mean ~~comes from GASBAG is set to zero~~ and the
prior slope is set to 0.0018 l/cm^{-1} while the associated uncertainties are set to 0.02 and ~~0.0000007~~ 7^{-7} l/cm^{-1} , respectively.

3.4 Measurement vector and error covariance

The measurement vector \mathbf{y} contains the radiance measurements with length $m = 4 \text{ bands} \times 1016 \text{ channels}$. For the $m \times m$
measurement and forward model error covariance matrix \mathbf{S}_ϵ ~~\mathbf{S}_ϵ~~ it is assumed that there is no error correlation between channels
so as a result it is diagonal such that $S_{\epsilon,b,c,c} = \sigma_{I_{b,c}}^2$ where $\sigma_{I_{b,c}}$ is from the noise model given by equation 7. In the GeoCarb

5 retrieval, as is common in many retrievals, the forward model error is not included due to the difficulty of characterizing this error which is assumed to be significantly less than the measurement error.

3.5 Pre-screening

Soundings that are unlikely to produce reliable L2FP results are filtered out. This is important since, due ~~the~~ to the large number of channels per sounding (4 ~~*~~ x 1016 = 4096 total channels), the L2FP algorithm is rather computationally intensive. This, 10 combined with the relatively large number of observations made on a daily basis, results in a significant computational burden. Therefore it is advantageous to avoid running it on soundings unnecessarily.

The first step in pre-screening is to of course skip soundings that are flagged as having radiances or supporting fields that are missing due to instrumental anomalies or L1B processing issues. Since the signal from soundings over ocean surfaces is too low to perform a successful retrieval and GeoCarb does not have a operational sun-glint mode these scenes will not be processed. 15 Ocean surfaces are identified using the land/water mask contained in the L1B file which is populated using the International Geosphere–Biosphere Programme (IGBP) land classification database (Townshend, 1992). Finally, soundings with aerosols and clouds that are too thick to produce a useful retrieval are filtered out. Aerosol and cloud filtering is performed using results from the A-band preprocessor (ABP) and the Generic Algorithm for the Single Band Acquisition of Gases (GASBAG), each discussed in the next two sections, respectively. The filtering is conservative so that inevitably there will be scenes where the 20 aerosol/cloud still might be too thick to yield a useful retrieval which will most likely be filtered out in the post processing filtering discussed in section 3.6.

3.5.1 A-band preprocessor

The A-band preprocessor (Taylor et al., 2012) performs an O₂ A-band retrieval using a fast forward model and assuming no aerosol or cloud; only molecular scattering. The spectrum is fit to the clear-sky model with five free parameters: surface 25 pressure P_s , an offset to the meteorological temperature profile, a spectral dispersion offset, and the surface albedo at the two band endpoints. Two quantities are then defined upon which to filter: $\Delta P_{s, \text{cld}}$ is the retrieved minus a priori surface pressure, and χ_R^2 is the ratio of the fit χ^2 , relative to the minimum χ^2 value possible at that same SNR. Scenes with $|\Delta P_{s, \text{cld}}| > 40$ hPa or $\chi_R^2 > 2.3$ are flagged as cloudy. The thresholds are set to be loose to filter only scenes where the aerosol/cloud is obviously ~~to~~ too thick.

30 3.5.2 Generic Algorithm for Single-Band Acquisition of Gases

The Generic Algorithm for Single-Band Acquisition of Gases (Somkuti et al., 2021) performs retrievals of ~~solar-induced fluorescence (SIF)~~ SIF and is the main processor for the GeoCarb operational SIF product L2GSB. In addition, it produces the so-called ratio retrievals which are used for aerosol and cloud screening, where independent single-band retrievals of ~~XCO₂ and XH₂O~~ XCO₂ and XH₂O in both the weak CO₂ and strong CO₂ bands are obtained by retrieving scaling coefficients of the prior gas profiles for both CO₂ and H₂O gases. Calculating the ratio of ~~XCO₂ and XH₂O~~ XCO₂ and XH₂O between the

5 values retrieved in both bands yields a value for each gas. In a completely cloud- and aerosol-free atmosphere the value will be close to unity. When aerosols and clouds are introduced, the photon path length can be different between the retrieval bands, as they are separated by roughly 0.4 μm . Since the retrieval approach is non-scattering, the only way for the forward model to adjust to the scattering-induced change in observed line depths is to scale the gas profiles, which ends up changing the ratio to be different from unity. Thus, the gas ratio provides an indicator for cloud and aerosol contamination in a measurement. The
10 minimum and maximum ratio thresholds are currently set to 0.8 and 1.5, respectively, for both gases.

3.6 Post-processing

The pre-screening filters out soundings with aerosols and clouds that are too thick from which to yield a useful retrieval but is aerosol/~~cloudy-conservative~~ cloud-conservative so there will be some soundings that still contain a small amount of aerosol and cloud. Of the soundings that pass the pre-screening and are processed with L2FP some fail to converge. This could be
15 due to the presence of ~~the thinner aerosols and clouds that went past pre-screener~~, limitations in the forward model to model the observed radiances with sufficient accuracy, and/or the fact that the inversion problem is ill-posed and nonlinear by nature making it difficult sometimes to optimally minimize χ^2 . Subsequently, there will be retrievals with X_{gas} results that have larger than expected errors compared to the 1- σ a posterior uncertainty from the retrieval due to scatter and/or systematic bias. A quality filtering procedure attempts to remove these problematic soundings. This is followed by a linear bias correction of
20 systematic errors to remove spurious dependencies in some variables on the retrieval. Both the filtering and bias correction steps essentially follow the methods described in O'Dell et al. (2018).

3.6.1 Filtering

Building filters is accomplished by selecting a training dataset and finding the variables that have the largest influence on the dataset by evaluating

$$25 \quad \Delta X_{\text{gas}} = X_{\text{gas,ret}} - X_{\text{gas,true}}, \quad (8)$$

where $X_{\text{gas,ret}}$ is the retrieved X_{gas} and $X_{\text{gas,true}}$ is what is considered the true X_{gas} . For an operational instrument the truth is obtained from one or more truth proxies which can be ground based observations, such as TCCON, or carbon flux inversion models. For a simulation study such as this one, the truth ~~can be~~ is computed from the measurement simulation inputs themselves. ~~The building process starts by first identifying the single variable that has the largest fraction of the variance in δX_{gas} from the training dataset. Then a threshold-based filter is created for this variable, the filter is applied, and the process starts over again to find the next most influential variable on δX_{gas} . This process is repeated until the variables that are left have a negligible influence on δX_{gas} . Building an optimal filter may require some trial and error as the optimal choice for thresholds is not immediately known and requires some intuition to choose, after applying the averaging kernel correction.~~ The filtering
5 is performed for ~~XCO₂, XCH₄, and XCO~~ XCO₂, XCH₄, and XCO together ensuring a consistent set of filtered soundings for each gas. Variables from L2FP, ABP, and GASBAG are all subject to being used in a filter threshold, and include not only state vector variables but variables derived from the retrievals. It is important to note that the optimal filter is not static. Changes

in L2FP inputs such as radiances (due to calibration changes), spectroscopic updates, updates in the meteorological modeling, and changes to the L2FP algorithm itself, will most likely require the production of a new [filterset of filters](#). This burden will subsequently be shown in this paper including the fact that this process can be a bit tedious but, as it turns out, that the process conveniently lends its self to machine learning techniques which are under investigation [Keely et al. \(2021\)](#) ([Keely et al., 2021](#))

3.6.2 [Bias correction](#)

The bias correction contains two terms: a parametric bias correction and a global bias correction. The bias correction for a particular sounding i is given as:

$$X_{i,\text{gas,ft,bc}} = X_{i,\text{gas,ft}} - C_p - C_g, \quad (9)$$

where $X_{i,\text{gas,ft}}$ is the filtered X_{gas} for sounding i , C_p is the parametric correction term, and C_g is the global correction term. The parametric bias correction has the form of a multiple linear regression following [Wunch et al. \(2011a\)](#) ([Wunch et al. \(2011b\)](#))

$$C_p = \sum_j^n c_j (p_j - p_{i,\text{ref}}), \quad (10)$$

where c_j are the regression coefficients, p_j are the selected parameters, and $p_{i,\text{ref}}$ are the parameter reference values. The parameters used are those that remove greater [that than 5%](#) of the variance relative to the global mean of the same truth proxies used to construct the filters. As with the filters, for this study the simulation inputs are used as [as the truth the truth, after the averaging kernel correction is applied](#). The set of parameters identified may be different with X_{gas} . It is important to note that, just as with the filters, the optimal set of parameters used for the parametric bias correction is not static and changes with changes in the input data and [algorithmic changes the algorithm](#). The global bias correction is simply the median difference between a sample set of filtered X_{gas} results and a matching sample set of true X_{gas} values from the truth proxy:

$$C_g = \text{median}(\mathbf{X}_{\text{gas,ft}} - \mathbf{X}_{\text{gas,true}}), \quad (11)$$

where $\mathbf{X}_{\text{gas,ft}}$ and $\mathbf{X}_{\text{gas,true}}$ are vectors whose elements are the set of samples.

30 4 Retrieval simulations and perturbation analysis

[To Up to this point, we have described the instrument, retrieval algorithm, pre- and post-filtering, and bias correction strategy of the retrieval approach. These are elements common to most other retrievals for GHGs and more generally remotely-sensed variables. In this section, we apply it to GeoCarb more specifically, to investigate how imperfect knowledge of several important parameters affects the L2 retrievals. To this end, bottom-up retrieval simulations with perturbations on those parameters were performed. In this section we We start by describing our scan strategy in section 4.1 which yields a set of scenes that covers most of the Americas at the peak of each season. We then describe the CSU Colorado State University \(CSU\) simulator in](#)

Table 5. Scan blocks that are used in the retrieval simulation experiments. Fields include the scan block number, name, size in the x and y directions N_x and N_y , the total number of soundings, minimum and maximum latitude/longitude at the middle of the scan block in the x/y directions, and the UTC times associated with the start and the end of the east–west scan of the north–south oriented slit.

Number	Name	N_x	N_y	Total #	Start/end lat	Start/end lon	Start UTC	End UTC
0	South America 2	241	1016	244856	-24.22 / 3.12	-33.39 / -53.15	14:45:00	15:19:00
1	South America 3	465	1016	472440	-41.93 / -11.31	-46.36 / -76.64	15:19:08	16:24:52
2	South America 1	601	1016	610616	-12.71 / 12.71	-48.92 / -82.18	16:25:01	17:50:01
3	North America	801	1016	813816	19.18 / 54.99	-69.31 / -121.51	17:50:09	19:43:29
4	Central America	601	1016	610616	7.00 / 35.01	-78.24 / -110.72	19:43:38	21:08:38

section 4.2 which produces the LIB ~~files and Met and Met files~~ used in our retrieval experiments. Finally, the setup for each L2 retrieval experiment is described in section 4.3, including details that are common to each experiment and, for each individual experiment, the perturbations made on the retrieval system inputs, and other relevant details specific to the experiment.

4.1 Simulation scan strategy

10 Since a formal GeoCarb scan strategy has yet to be determined, for ~~the these~~ retrieval experiments a ~~simple~~ strategy was created that consists of five scan blocks that cover the land in the full disk that will most likely be covered by GeoCarb. The SSP is set to ~~8587°~~ west longitude, which ~~is different than the currently planned SSP of 103° west longitude, which, in fact, is subject to change when the host platform for GeoCarb is finalized. Four sets gives good coverage of both North and South America. Four days~~ of five scan blocks are included: March 21, 2016, June 21, 2016, September 21, 2016, and December 21, 2016, each
15 corresponding approximately to a seasonal equinox or solstice, for a total of 20 scan blocks. They cover most of the Americas with a highest and lowest latitudes at approximately 60° and -42°, respectively. The scan blocks are listed in table 5, in the order in which they are scanned, including their number, name, size in the x and y directions, the total number of soundings, minimum and maximum latitude/longitude at the middle of the scan block in the x/y directions, and the UTC times associated with the start and the end of the east–west scan of the north–south oriented slit. The scan start times were picked to minimize
20 the overall mean solar zenith angle and airmass, ~~and therefore the SNR,~~ for all five blocks together.

The scan blocks are illustrated in figures 2 and 3 for the June 21, 2016 and December 21, 2016 cases, respectively. Three maps of the Earth disc visible by GeoCarb at an SSP of ~~8587°~~ west (marked by the thick black ‘X’) are shown. From left to right, the first shows the satellite zenith angle θ . It is clear that the satellite zenith angle increases radially away from the SSP or towards the outside of the Earth disk which is inherent in a geostationary orbital configuration and a distinguishing characteristic from nadir looking instruments such as OCO-2/3. This is important because the plane parallel assumption used in the RT in the retrieval forward model breaks down as the satellite zenith angle increases ~~and ultimately decreasing SNR~~. The satellite zenith angles for scenes over land used in this study range from 7.54 to 78.06°. It is expected that, depending on other

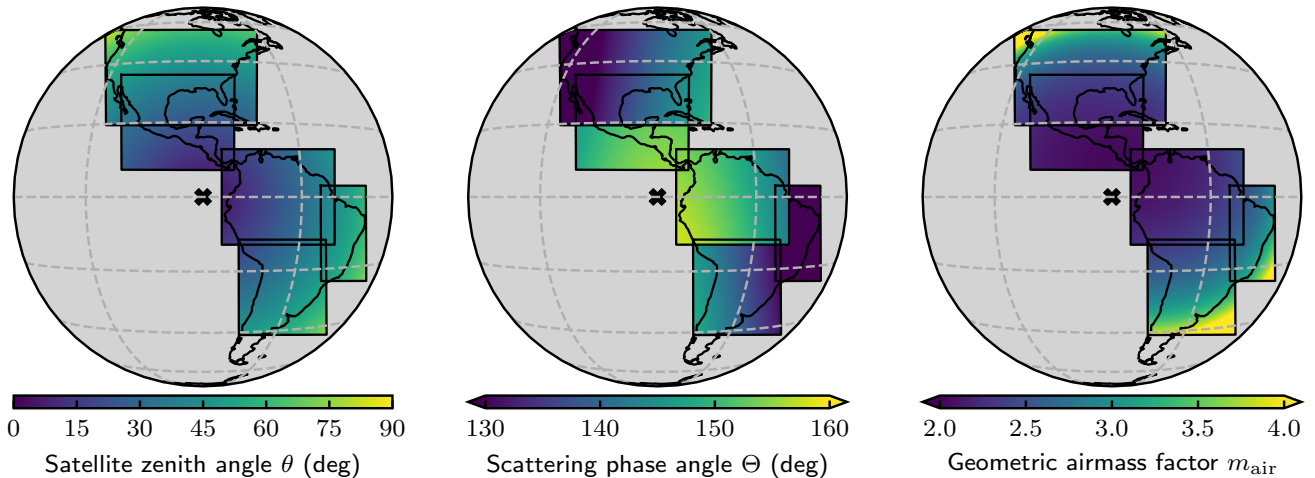


Figure 2. Maps of three key retrieval input variables for June 21, 2016 plotted in the five scan blocks used for the retrieval simulation experiments. The 'X' at the center of the geostationary projection shows the GeoCarb sub-satellite point at 87° west.

5 scene characteristics, aerosol optical thickness and airmass path, scenes with larger satellite zenith angles will more likely be candidates to be filtered.

Analogously, large solar zenith angles are also be-problematic in the RT calculations. The solar zenith angle for GeoCarb scenes will depend on a combination of location and time with earlier or later local observation times having larger solar zenith angles. It is important that the finalized scan strategy is optimized for-SNR-by minimizing the mean solar zenith angle. In contrast, since since OCO-2 is in a sun synchronous orbit the solar zenith angles for OCO-2 observations are usually relatively low and consistent.

The second map from the left shows the single scattering phase angle Θ of single scattered photons reaching the instrument, which, by the spherical law of cosines, is given by the following relation:

$$\cos \Theta = - \left(\cos \theta_0 \cos \theta + \sin \theta_0 \sin \theta \cos(\phi - \phi_0) \right), \quad (12)$$

15 where θ_0 and θ are the solar and satellite zenith angles and ϕ_0 and ϕ are the solar and satellite azimuth angles, both clockwise from north. The single scattering phase angle is the input to the single scattering phase function $P(\Theta)$ which is the distribution of scattering from a molecule or particle such that $\Theta = 0^\circ$ is forward scattering and $\Theta = 180^\circ$ is backscattering. In the backscattering case the instrument would be viewing the so-called “hot-spot” but for GeoCarb, with the SSP over ocean (both at the currently planned 103° west longitude and the 8587° used for this study), hot-spot geometry will not be encountered for soundings over land. The single scattering phase angle is important as, The phase angles for scenes over land used in this study range from 106.6 to 176.8° and depend on location due to satellite zenith angle but also on the observation time due to solar zenith angle which is apparent in the variation in phase angle with scan blocks scanned at different times.

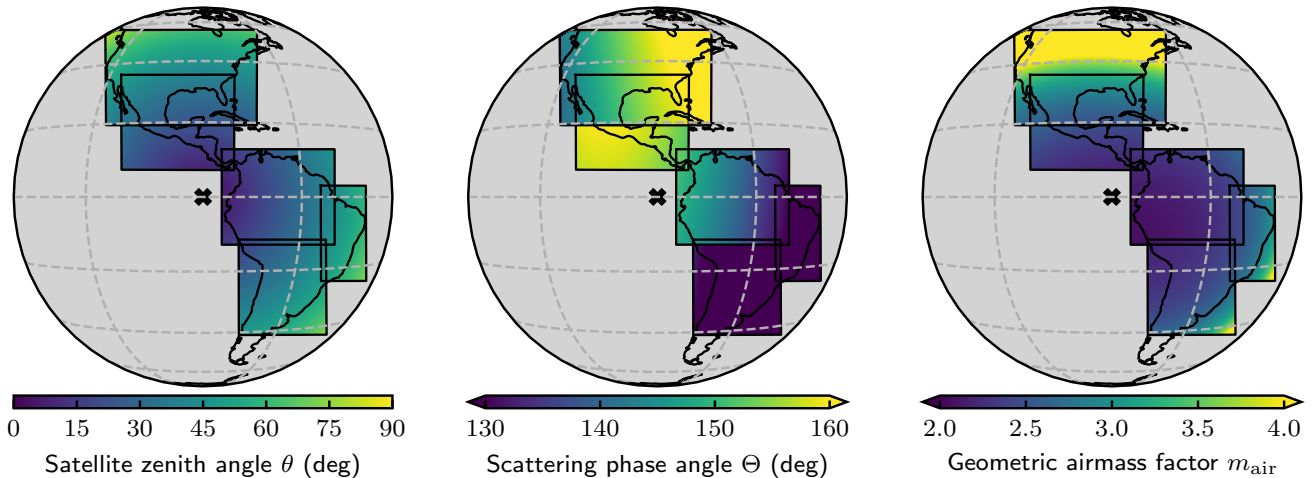


Figure 3. Same as figure 2 but for December 21, 2016.

Finally, the third map from the left shows the airmass factor m_{air} in a plane-parallel atmosphere given by

$$m_{\text{air}} = \frac{1}{\cos\theta_0} + \frac{1}{\cos\theta}. \quad (13)$$

25 The airmass factor is the *direct* optical path length of solar radiation incident at TOA that is scattered once in the atmosphere or at the surface into a direct path back to TOA and measured by an instrument sensor, relative to the optical path for vertically incident and vertically scattered radiation, i.e. when $\cos\theta_0 = 0$ and $\cos\theta = 0$. The airmass factor is important from a RT perspective in that as it increases the plane-parallel assumption starts to break down increasing error in the forward model while also the amount of aerosols and clouds in the direct path will increase which increases the contribution of light reflected from aerosol/cloud in the upper troposphere relative to light reflected from the ground. This ~~decreases-SNR-and~~ makes it less likely the inversion will produce a useful retrieval passing the post processing filters. In fact, the airmass factor itself is used as a filter variable (see figure 4.8) with a maximum threshold of 4.2. The airmass factors for the land scenes used in this study range from 2.01 to 13.00 indicating that at least some retrievals will not meet the maximum airmass factor threshold.

Due to the number of retrieval experiments performed the current GeoCarb spatial resolution of 2.7 km N-S and 5.4 km E-W would be computational prohibitive so the resolution was down-sampled by a factor of 20 N-S \times 10 E-W, $\approx 0.5^\circ \sim 0.5^\circ$. Our goal is to study the retrieval system over a wide range of conditions and we are not concerned about spatial coherence between neighboring pixels. Since the geographic range of our dataset covers that which GeoCarb ~~will ultimately sample~~ would have samples, we believe that even with the down sampling our dataset will cover an adequate range of conditions. After down sampling the number of soundings per season is 13,812 for a total of 55,248 soundings for all four season which can be compared to the original numbers before down sampling of 2,752,344 per season for a total of 11,009,376 soundings.

4.2 CSU simulator

10 The CSU simulator takes as input meteorological, trace gas, cloud and aerosol, and surface parameters for each individual scene based on location and time along with instrument parameters and produces L1B files which include synthetic radiometric measurements along with their time, geolocation, solar/satellite geometry, instrument characteristics, and other parameters associated with the measurements. In addition, the simulator produces Met files associated with each scene which contain meteorological prior parameters that ~~can be~~ are used in the L2 ~~retrieval~~ retrievals. The simulator was originally developed for
15 OCO-1 while support for OCO-2/3, and GOSAT were subsequently added followed by support for GeoCarb. The simulator is discussed in detail in various references ~~O'Brien et al. (2009); Polonsky et al. (2014)~~ such as O'Brien et al. (2009) or P2014 and will only be summarized here.

The simulation process can essentially be divided into three steps:

1. Produce the geolocation and solar/satellite geometry for each scene based on scan block definitions including the starting
20 epoch, SSP, target (scan block center) latitude/longitude, number of north–south (currently fixed at 1016 footprints along slit) and east–west FOVs, and north–south/east–west sample increment.
2. For each scene, collect and interpolate from various sources the trace gas, meteorological, aerosol/cloud, and surface parameters for input into step three, referred to as the scene input, and to produce “truth” Met files.
3. Take the information produced in steps one and two along with scene independent instrument characteristics such as
25 the Stokes coefficients, the ILS table, and noise coefficients to run the forward model that produces synthetic radiance measurements.

The simulator is well documented in O'Brien et al. (2009) and P2014. Changes relative to those references include updates discussed in section 1 including the instrument model details discussed in section 3.2.1. We would like to refer the interested readers to these references for further details. It should be noted that the simulator does not account for the other instrument
30 effects discussed in section section 2. In addition, the effects of scene inhomogeneity are also not taken into account and therefore ILS variation across the scene is ignored. In the end these effects will be important to rectify, for which there is ongoing research.

4.3 Experimental setup

In this section perturbation analysis experiments are presented, where perturbations are made on several key inputs to the L2
5 retrieval system. These perturbations will affect the entire system including pre-processing (ABP and GASBAG), L2FP, and post-processing, and allow us to construct an error budget for GeoCarb given the uncertainties investigated (unmodeled effects notwithstanding). Following is an outline of the steps involved in producing results for each experiment:

1. Produce baseline L1B input with the CSU simulator on the full set of scenes that result from the scan strategy described in section 4.1. This occurs before pre-processing so it includes scenes over ocean and scenes that will have too much
10 aerosol/cloud to produce a reliable L2FP retrieval.

2. ~~Apply the averaging kernel correction to the truth for comparison to each experiment's results later. The truth comes from the scene input to the RT component of the simulator.~~

3. For each experiment perform the following steps:

(a) If required, perturb one or more variables in the L1B input as appropriate.

15 (b) Run pre-processing including filtering out scenes over ocean and running ABP and GASBAG and subsequently screening for clouds. Note that ABP and GASBAG results will also be used for the post-process filtering.

(c) Run the L2FP retrieval with the perturbed inputs. Depending on the experiment the perturbed inputs may be the L1B input and/or the spectroscopy and/or meteorology inputs.

(d) Apply Tailor and apply the post-process filtering and bias correction to the L2FP X_{gas} results.

20 (e) Apply the averaging kernel correction to the truth for comparison to each experiment's results. The truth comes from the scene input to the RT component of the simulator.

(f) Analyze the differences in X_{gas} between the truth ~~provided by simulation step two~~ and that retrieved by L2FP.

Since GeoCarb ~~will not~~ was not meant to perform retrievals over ocean, all soundings over ocean are filtered out for the L2 retrievals as discussed in section 3.5. This process results in reduction of the number of soundings to simulate to 8278 for each season for a total of 33111 soundings. Since all but one of our experiments are performed with an atmosphere containing aerosols and clouds, the aerosol and cloud screening discussed in section 3.5 is performed on all simulated soundings over land. This results in a further reduction in the number of soundings to perform retrievals on for each season to 3104 for a total of 12520 soundings. Note that after the retrieval is performed ~~there will of course,~~ there will be an additional reduction in the number of retrievals used in the analysis due to the filtering post-filtering discussed in section 3.6.

30 There are a few differences in the L2FP runs for the experiments compared to the planned mission configuration presented in section 3. At the time of this writing, the GeoCarb instrument has yet to undergo a formal instrument characterization of polarization, the ILS, or noise characteristics so for the experiments in this study the Mueller matrix, the ILS, and the noise coefficients are based on known characteristics of the optical components and optical model calculations of the instrument as a whole. ~~The prior profiles for CH₄ and CO are from~~ These make them particularly different from the truth fields, and hence the retrieval is truly challenged in this regard. For aerosol, the same aerosol types are used but the aerosol optical thickness prior comes from the aerosol climatology of the Modern-Era Retrospective analysis for Research and Applications (MERRA) (Rienecker et al., 2011). For the surface BRDF, the quadratic term is not included. Since the L1B simulations only include a linear variation in wavelength leaving the quadratic term out in the L2FP retrievals will ~~have~~ not affect the outcome of the experimental results. Finally, it was judged not to ~~included EOFs for the~~ include EOFs for these experiments since for the baseline both the L1B simulations and the L2FP retrievals use the same spectroscopic tables, solar model, and instrument characteristics, and that the effects of the perturbations applied in the experiments would be easier to decipher without the effects of applying EOFs. Therefore, we expect our results to be conservative, in that EOFs should only serve to reduce systematic errors (O'Dell et al., 2018).

5

10 4.3.1 Baseline Experiments

To establish a “baseline” for comparison we ran the retrieval system with nothing perturbed, i.e. with perfect knowledge of the experimental inputs. In this case, both the L1B simulations and the ABP, GASBAG, and L2FP retrievals use the same set of input parameters of interest. Even though these input parameters are the same, there are still differences in the simulator and L2FP that will result in X_{gas} retrieval errors relative to the “truth” computed from the simulator inputs. The differences include different aerosol/cloud models, different surface BRDF models, different SIF models, differences between the prior and truth profiles of CO₂, CH₄, and CO, differences in the layer discretization of the atmosphere, and subtle differences in the forward model RT. Errors relative to truth also arise from the OE inversion including the choice of additional priors and algorithmic controls and the ability for the algorithm to minimize the differences between the measurements and the forward model since the inversion problem is ill-posed and nonlinear by nature.

In addition to the baseline test described above, we performed two other tests with modifications to the baseline. First, the L1B simulator is ran without aerosols and clouds included. Although unrealistic, this test shows the effects of aerosols and clouds on the baseline test and on post process filtering. In addition, baseline L1B files with synthetic noise added are produced, for the case including aerosols and clouds. This does not require a separate simulator run as the synthetic noise can simply be added to the radiances in the L1B files. Using the GeoCarb noise model and assuming a Gaussian noise distribution the radiance with noise $I_{N,b,c}$ for band b and channel c can be written as

$$I_{N,b,c} = I_{b,c} + \sigma_{I_{b,c}} \times \text{RN}(\mu, \sigma), \quad (14)$$

where $I_{b,c}$ is the radiance without noise, $\sigma_{I_{b,c}}$ is the standard deviation of the noise given by equation 7, and $\text{RN}(\mu, \sigma)$ returns a random sample from a “standard normal” distribution with a mean $\mu = 0$ and standard deviation $\sigma = 1$. For the rest of the experiments random noise is not included as including random noise simply widens the bias distribution by the width of the random uncertainty. ~~It was thought that without random noise the effects of the experimental perturbations would be easier to spot in the narrower error distributions.~~

4.3.2 Perturbation Experiments

20 We performed seven different experiments, each introducing imperfect knowledge, relative to the baseline run, of one or more parameters. The experiments include imperfect knowledge of radiometric calibration, ILS, polarization, pointing, spectroscopy, meteorology, and an imperfect knowledge of all the parameters. These tests along with the baseline runs described above are summarized in table 6.

1. Radiometric calibration of the instrument, ~~or the i.e.,~~ radiometric gain, is the factor applied to the measured voltages to convert them to absolute physical units. This is a per channel scale and offset that should not be confused with random noise in the measurements. The For GeoCarb, the absolute radiometric performance requirement of all spatial samples across the full FOV and across the full spectral range of the four channels is an uncertainty that is no larger than 5% (GeoCarb MDRA, 2020) so that for the radiometric calibration experiment we introduced imperfect knowledge simply

Table 6. The experimental runs with or without aerosol/cloud (a/c), with or without noise, and with the given perturbations (pert.) applied on the baseline run.

Run #	Run name	Perturbation	# of runs	Notes
1	No a/c	none	1	Aerosol and cloud not included in L1B simulation.
2	With (W) a/c	none	1	The standard run for comparison.
3	W. a/c, with noise	+ radiance noise	1	Gaussian noise added using the GeoCarb noise model.
4	W. a/c, pert. rad. cal.	$\times 1.05$	4	Multiplicative factor on radiance, each band separately and all bands.
5	W. a/c, pert. ILS	$\times 1.01$	4	Multiplicative factor on ILS $\Delta\lambda$, each band separately and all bands.
6	W. a/c, pert. polarization	No polarization	4	All elements of the retrieval Muller matrix zeroed except (1,1), each band separately and all bands.
7	W. a/c, pert. pointing	Target shift	1	Shift the SSP resulting in a 1 km shift westward of the center of each observation.
8	W. a/c, pert. meteorology	Dif. met forecast	1	GEOS-5 instead of ECMWF.
9	W. a/c, pert. spectroscopy	Old spectroscopy	1	Old spectroscopy tables, HITRAN-2008 instead of HITRAN-2016.
10	W. a/c, pert. kit. sink	Perts.: 4, 5, 6, 8, 9	1	All perturbations together and for all bands, except #7.
11	W. a/c, pert. kit. sink, with noise	Perts.: 4, 5, 6, 8, 9	1	All perturbations together and for all bands, except #7.

by scaling the radiances in the L1B files by a factor of 1.05. We performed this experiment for each band separately and for all bands together in an attempt to reveal differences in the sensitivity to radiometric calibration between bands.

2. We introduced imperfect knowledge of the ILS by modifying the ILS given in the L1B files. The ILS is provided for each footprint, band, and channel as a table of n points as a function of delta wavelength $\Delta\lambda$ from the center of the ILS ranging from $-\Delta\lambda$ to $\Delta\lambda$. By multiplying the $\Delta\lambda$ vector by a scale factor, effectively scaling the FWHM, the ILS is either stretched or squashed making it broader or narrower, respectively. For this we used a scale factor of 1.01 which results in a perturbation that is larger than matches the current FWHM uncertainty requirement of 0.2% GeoCarb MDRA (2020) (GeoCarb MDRA, 2020). We performed this experiment for each band separately and for all bands together. It should be noted that for this perturbation experiment, we took the per-band ILS scaling factor out of the retrieval state vector.

~~For polarization induced by the instrument optics and incident on the detector-~~

3. For polarization, we introduced imperfect knowledge ~~by modifying the input L1B files so that of the polarization sensitivity of the instrument by having~~ the L2 retrieval simply ~~assumes assume~~ that there is no polarization, i.e. $S(\lambda) = [I, 0, 0, 0]$. Eliminating the polarization knowledge can be done by setting all but the (1,1) element of the Muller matrix

10 M in equation 4 to zero so therefore the Q , U , and V components of the Stokes vector S are ignored in the forward model RT calculations. We performed this experiment for each band separately and for all bands together. [This test is actually a repeat of the same test performed in O2015, but using our updated simulation/retrieval framework and GeoCarb instrument model.](#)

4. Instrument pointing errors, caused by errors in the knowledge of spacecraft attitude and/or the orientation of the optical scan mirrors, result in errors in the geolocation, solar/satellite geometry, and polarization rotation, associated with the measurements. Knowledge of the geolocation is important for determining atmospheric and surface priors that are a function of location including surface pressure which is subsequently dependent on a particular location's elevation. ~~In~~ addition, knowledge of the solar/satellite geometry and polarization rotation are used for the RT calculations in the forward model. The pointing perturbation was accomplished simply by shifting the SSP 0.009579 degrees west in longitude (from 87W to 87.009579W longitude) which has the effect of inducing a roughly 1 km westward shift of the center of each ~~observation point~~ [2.7 × 5.4 km footprint](#).

5. [For meteorology we introduced imperfect knowledge by using meteorology from a different forecast model. As a reminder, for the baseline simulations we used the ECMWF forecast described in section 4.2. For this experiment we used meteorology from the GEOS-5 FP-IT forecast. This is the source for meteorology planned for the operational GeoCarb L2FP retrieval as described in section 3.2. It is assumed that the variations between these two different models will represent a theoretical ensemble uncertainty in model results, whether from different models or different versions of those models.](#)

6. We introduced imperfect knowledge of spectroscopy by using an older version of the spectroscopic reference tables than that used for the baseline L1B simulation and the baseline L2FP retrieval. The older O₂ and CO₂ spectroscopic data comes from the same research for the OCO-2/3 projects as discussed in section 3.2 but significantly pre-dates that used for the current L2FP retrieval. The data for H₂O, CH₄, and CO are based on HITRAN-2008 (Rothman et al., 2009) rather than HITRAN-2016. We believe that this table replacement is sufficient to introduce imperfect knowledge due to spectroscopic parameters such as: line strength, air broadening, ~~T-width, CIA~~ [temperature dependence, collision-induced absorption](#), H₂O broadening, pressure shift, line mixing, and speed dependence, since it is these parameters that continually get improved with on going spectroscopic research.

~~For meteorology we introduced imperfect knowledge by using meteorology from a different forecast model. As a reminder, for the baseline simulations we used the ECMWF forecast described in section 4.2. For this experiment we used meteorology from the GEOS-5 FP-IT forecast. This is the source for meteorology planned for the operational GeoCarb L2FP retrieval as described in section 3.2. It is assumed that the variations between these two different models will represent a theoretical ensemble uncertainty in model results, whether from different models or different versions of those models.~~

The experimental runs with or without aerosol/cloud (a/c), with or without noise, and with the given perturbations (pert.) applied on the baseline run:

- 15 7. The “kitchen sink” includes all perturbations 1–7 above except for the single day of pointing perturbation.

4.3.3 Averaging Kernel Correction

In order to properly compare the retrieved X_{gas} to the true value, the averaging kernel matrix from the retrieval is used to construct a gas profile $\mathbf{u}_{\text{gas,ak}}$ that is comparable to the retrieved profile in that it contains influence from both the true profile and the prior profile in the same proportions as the retrieved profile:

$$\mathbf{u}_{\text{gas,ak}} = \mathbf{A}_{\text{gas}} \mathbf{u}_{\text{gas,true}} + (\mathbf{I} - \mathbf{A}_{\text{gas}}) \mathbf{u}_{\text{gas,a gas,ap}}, \quad (15)$$

- 5 where \mathbf{A}_{gas} is the averaging kernel matrix for a particular gas, $\mathbf{u}_{\text{gas,true}}$ is the true gas profile, which in this case is from the simulation scene input from step 2 in the simulation process, $\mathbf{u}_{\text{gas,a gas,ap}}$ is the prior gas profile, and \mathbf{I} is the identity matrix.

~~The X_{gas} error is then given by~~

$$\Delta X_{\text{gas}} = \hat{X}_{\text{gas}} - \mathbf{h}^T \mathbf{u}_{\text{gas,ak}} = \hat{X}_{\text{gas}} - X_{\text{gas,ak}},$$

We then convert this to the column integrated fraction as

10
$$\begin{aligned} X_{\text{gas,ak}} &= \mathbf{h}^T \mathbf{u}_{\text{gas,ak}} \\ &= X_{\text{gas,true}} + (\mathbf{h} - \mathbf{a}_{\text{gas}})^T (\mathbf{u}_{\text{gas,ap}} - \mathbf{u}_{\text{gas,true}}), \end{aligned} \quad (16)$$

where \hat{X}_{gas} is the retrieved gas profile, $\mathbf{a}_{\text{gas}} = \mathbf{h}^T \mathbf{A}_{\text{gas}}$ is the (un-normalized) averaging kernel vector for the gas in question, and the pressure weighting function \mathbf{h} is defined by the pressure level intervals in the profile normalized by the surface pressure and is provided with the L2FP results. The X_{gas} retrieval error is then given simply by

15
$$\Delta X_{\text{gas}} = \hat{X}_{\text{gas}} - X_{\text{gas,ak}}, \quad (17)$$

where \hat{X}_{gas} is the retrieved gas column integrated fraction. The averaging kernel matrix \mathbf{A}_{gas} , prior profile $\mathbf{u}_{\text{gas,a gas,ap}}$, and pressure weighting function \mathbf{h} are all obtained from the L2FP output at 20 levels and are ~~therefore then~~ interpolated to the 72 levels of the true profile $\mathbf{u}_{\text{gas,true}}$. Unless otherwise stated, this is how the errors are determined in the various retrieval experiments.

- 20 A brief discussion on this “AK Correction” is warranted. The averaging kernel vector \mathbf{a}_{gas} , given by equation ??, quantifies the response of the retrieved X_{gas} to changes in the true gas profile, which can be written as

$$\mathbf{a}_{\text{gas},j} = \frac{\partial X_{\text{gas}}}{\partial \mathbf{u}_{\text{gas,true},j}}, \quad j = 1..n, \quad (18)$$

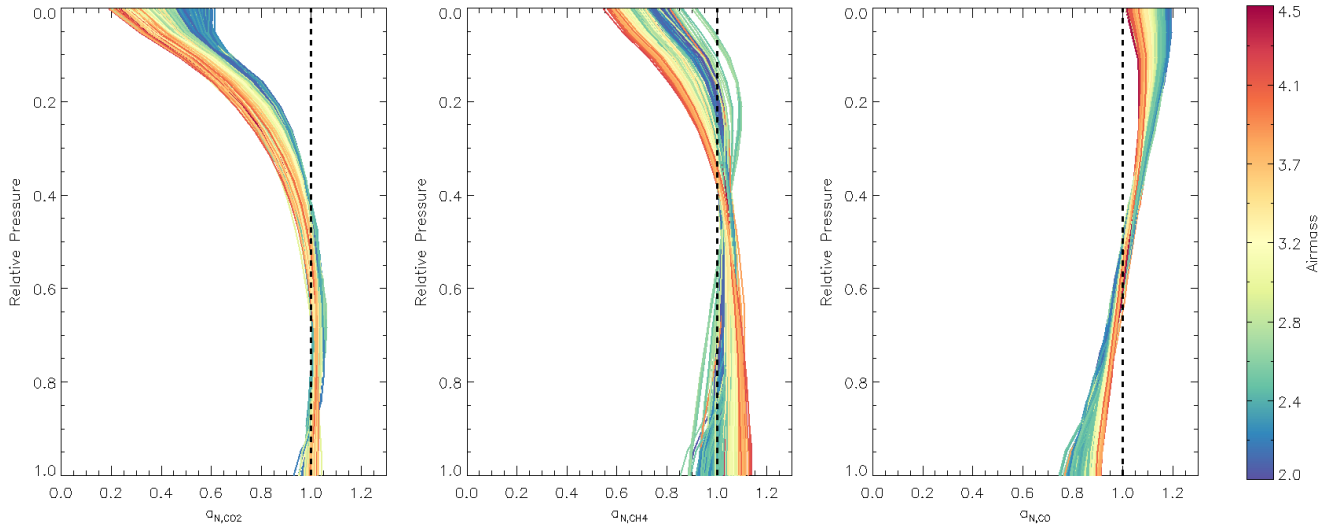


Figure 4. Normalized averaging kernel vectors \mathbf{a}_N for X_{CO_2} , X_{CH_4} , and X_{CO} for all soundings passing our quality flag (Section 5.1), colored by airmass factor.

where n is the number of vertical levels. This quantity is straightforward to derive from the full retrieval averaging kernel matrix \mathbf{A} and several other quantities (see, e.g. Connor et al., 2008). It is common to normalize this quantity with respect to the pressure weighting function :

$$\mathbf{a}_{N,\text{gas},j} = \frac{\mathbf{a}_{\text{gas},j}}{h_j}. \quad (19)$$

This normalized averaging kernel vector can have values from below 0 to greater than 1. A value of unity means that a given change in the true gas profile causes a fully proportional change in the retrieved gas column fraction, i.e., there is no influence from the prior. For a perfect retrieval with perfect sensitivity, the values would all be unity.

Figure 4 shows the normalized averaging kernel vectors for X_{CO_2} , X_{CH_4} , and X_{CO} for our GeoCarb simulations, taken for all soundings that pass the post-retrieval quality flag in the baseline experiments (Section 5.1). From the figures it can be seen that the sensitivity to CO_2 and CH_4 is larger closer to the Earth's surface, and is generally a function of airmass. This is as expected and optimal for the GeoCarb mission due sensitivity to sources and sinks at the surface. On the other hand, there is generally a slight increase in sensitivity to X_{CO} with altitude. These AKs are very similar to their uplooking counterparts from TCCON (e.g. Wunch et al., 2011a, Fig. 4)

5 Results

In this section results are presented for each experiment in the order listed in table 6. Though the GeoCarb mission requirements have no formal requirement on accuracy, we will take the multi-sounding precision requirements to similarly apply to accuracy.

That is, we will typically evaluate the mean and standard deviation of the error for a given gas column fraction, and require both to be less than the requirements given in Table 1.

There are two important details about the sounding selection process in the presentation:

- There will be a certain amount of soundings that did not converge in the inversion process discussed in section 3.1 which are not included in the analysis. These soundings did not converge, either due to too much aerosol and/or cloud and did not get filtered out in the pre-screening process or have other physical attributes that are not adequately represented in the forward model.
- The results presented are the intersection of the set of baseline results with the set of results of the particular experiment. This means that only soundings that converged in both cases are shown. As a result, the presentation of the baseline results will contain the most amount of soundings and all other cases will contain as many or less than that of the baseline results.

Results are shown for three cases: unfiltered (“Raw”), filtered (“Filtered”), and filtered and bias corrected (“Filtered + BC”).

The statics presented include: the number of soundings n in the plot, the mean error μ , and the standard deviation of the errors

σ .

5.1 Baseline

Figures 5 and 6 present histograms of retrieval errors for X_{CO_2} , X_{CH_4} , and X_{CO} for the baseline case, i.e. perfect knowledge of all variables investigated, for the special case with aerosols and clouds artificially removed (clear-sky) and in the case with aerosols and clouds included (all-sky), respectively. It is clear that the errors in the clear-sky case are significantly less compared to the all-sky case. This is as expected and is really a sanity check for the simulation system. The percentage of soundings making it through the filters in the clear-sky case (95.4%) is significantly higher than in the all-sky case (68.1%). This is consistent with what we have already discussed in section 3.6 in that the filtering process is designed to remove retrievals that are not reliable due to the presence of aerosols and clouds.

It is not surprising that the filtered and bias corrected clear-sky retrievals meet the mission accuracy-precision requirements listed in table 1 (even the raw unfiltered results meet the requirements) but the all-sky filtered and bias corrected results also meet the accuracy requirements with errors of -0.05 ± 0.70 ppm, 1.08 ± 6.59 ppb, and -0.02 ± 0.79 ppb for X_{CO_2} , X_{CH_4} , and X_{CO} , respectively. These are of course the results for the case of perfect knowledge of the variables investigated and with no random noise added. It is apparent from the plots that the retrievals of X_{CO_2} and especially X_{CH_4} , are driven primarily by systematic errors, which does not seem to be the case for X_{CO} . The large median bias in X_{CH_4} of -6.59 ppb is interesting and we are not certain of the origin driving this. This may be effects from the spectroscopy that are not fitted for in the retrieval. It is possible that including EOFs in the retrieval as discussed in section 3.3 will account for some of this bias, although it turns out that curious, and may be due to a significant bias in the X_{CH_4} prior (mean bias ~ 40 ppb). Any mean biases for these gas columns are largely removed by the bias correction.

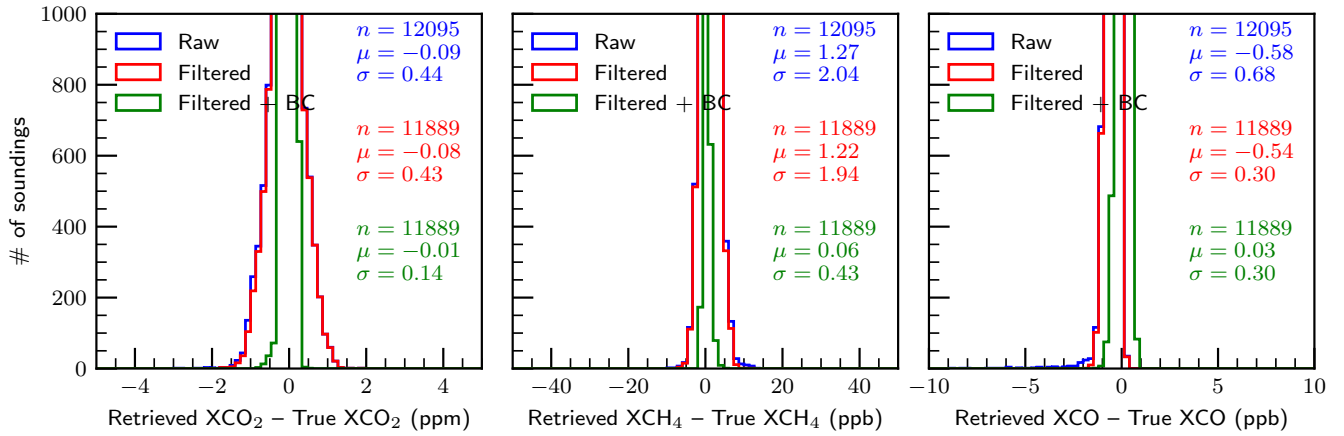


Figure 5. Baseline retrieval error results without clouds and aerosols (clear-sky) for three cases: unfiltered (raw), filtered, and filtered and bias corrected (BC). Statistics include: the number of soundings n , the average error μ , and the standard deviation of the errors σ .

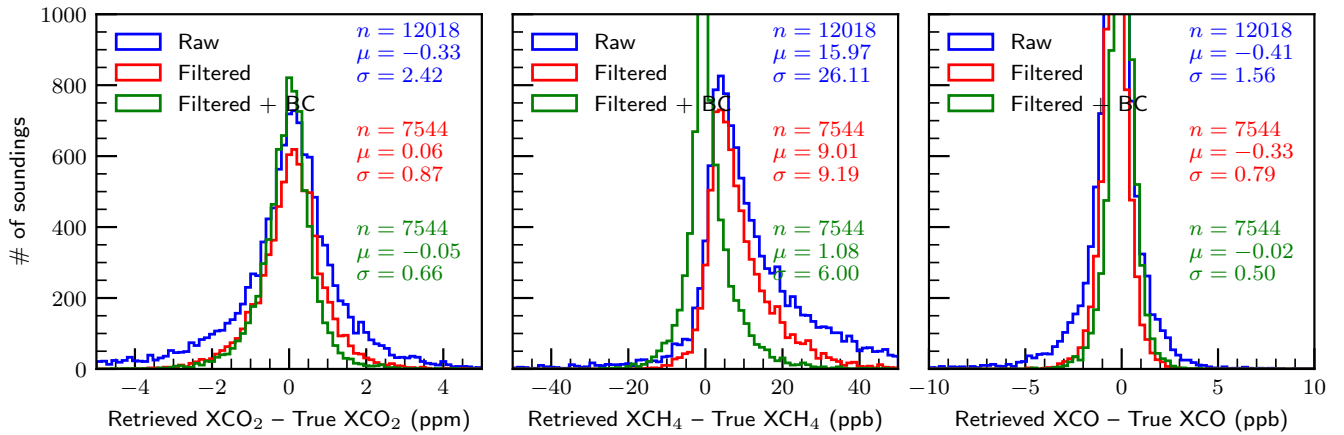


Figure 6. Same as figure 5 but with clouds and aerosols (all-sky).

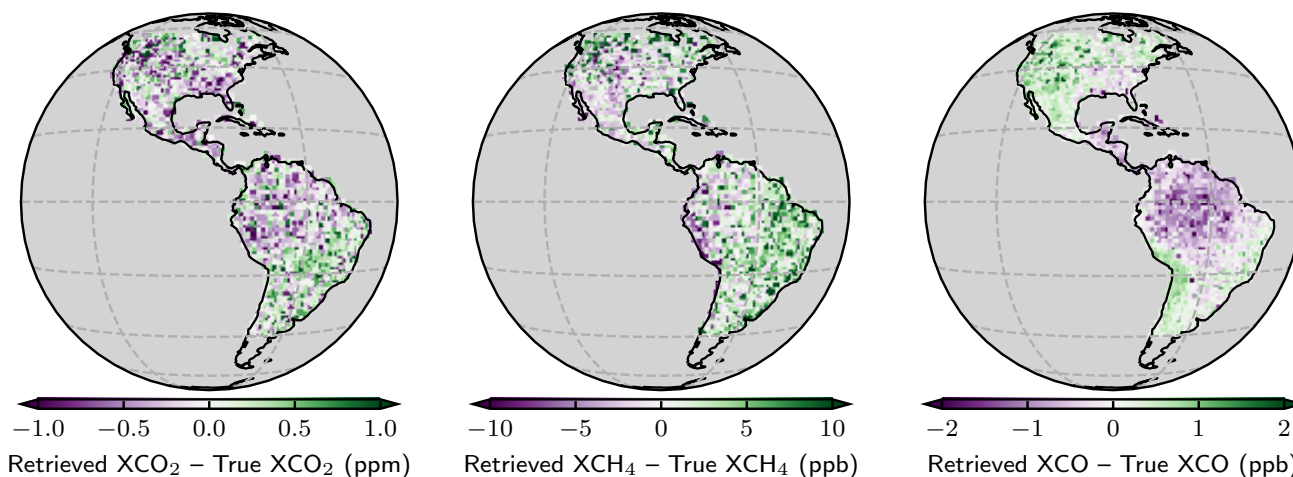


Figure 7. Maps of same results shown in figure 6 for the filtered and bias corrected case.

Maps of the all-sky baseline results are shown in figure 7 for the filtered and bias corrected case. Features include positive biases in X_{CO_2} and X_{CO} at larger satellite zenith angles leading to larger SNRs. Negative biases are apparent in X_{CH_4} over high altitude areas due to difficulty retrieving in these areas, although it is unclear why this is only apparent in X_{CH_4} for methane. Finally, small negative biases in X_{CO} of order -1 ppb are prevalent over the Amazon, likely due to persistent cloud cover that either has not been pre-screened out or caught by the filtering.

The

25 5.1.1 Quality Filtering

The post-retrieval filtering approach is demonstrated in figure 8, which shows X_{CO_2} vs the filtering parameters with the simulation inputs as the truth proxy. The top twelve most important filters are shown sorted by importance from left-to-right and then from top-down. Table 7 summarizes the results for all three gases. It is apparent that just a few variables do the bulk of the filtering and that overall the filter variables are almost always associated with negative biases in X_{CO_2} and positive biases in X_{CH_4} .

The variable with the largest filtering effect ($\approx 21\% \sim 21\%$ of the soundings filtered out) is the H_2O ratio from GASBAG which filters out scenes with too much cloud and aerosol contamination. The CO_2 ratio is also a filter variable which also indicates cloud and aerosol contamination but has much less of an effect than the H_2O ratio. Another important filter variable is $\Delta P = \hat{P} - P_{\text{true}}$, where \hat{P} is the retrieved surface pressure from either the L2FP retrieval or the ABP retrieval. The importance of these variables this variable is most likely due to photon path length related errors effects from aerosols and clouds and the retrieval adjusting ΔP to compensate. The retrieved AOT aerosol optical thickness (AOT) is also an important filter variable, specifically for the larger aerosol types including dust (DU) and ice cloud (ice), and the total AOT for all aerosols and clouds.

Large values of dust AOT are particularly associated with large negative biases in X_{CO_2} due to the increased sensitivity to large particles in the CO_2 bands relative to that to smaller particles. In contrast, ice crystal particles become a more important filter for large X_{CH_4} and X_{CO} biases (not shown) due to ~~the a~~ larger sensitivity of the X_{CH_4} band to ~~relatively large~~ ice crystals. The X_{CH_4} retrieved uncertainty filters out retrievals with significant scatter although any specific source of this scatter is unknown. The CO_2 vertical gradient delta is defined as the difference in retrieved X_{CO_2} between the surface and the retrieval pressure level at 0.7 times the surface pressure minus the same quantity for the prior given by

$$\text{co2_grad_del} = [c(1) - c(0.7)] - [c_a(1) - c_a(0.7)], \quad (20)$$

10 where $c(x)$ and $c_a(x)$ are the retrieved and a priori CO_2 dry air mole fraction, respectively, at relative pressure x . ~~It is unclear why this filter variable is associated with bias and scatter which is currently being investigated.~~ Sounding altitude is a filter variable which may normally be attributed to pointing errors but since knowledge of the pointing in the baseline results is “perfect” the altitude may be a proxy for difficulties in making retrievals at high altitudes, including errors in the prior surface pressure, broken clouds, and/or the presence of snow/ice. The band 2 ILS scaling filter most likely indicates the case where an effect is not accounted for in the forward model with the ILS scaling compensating for it. The filtering finishes off with the airmass factor m_{air} , which is influenced by both the solar and satellite zenith angles, where large angles result in an increase in scattering effects and associated larger RT errors.

5 It must be noted that new filters *usually* need to be rebuilt when changes are made to the retrieval system. These changes include changes made to the radiances (~~do due~~ to calibration changes), spectroscopy, prior inputs, and finally the forward model physics. In the past, for OCO-2/3, new filters have been produced with each release of the L2FP product (O’Dell et al., 2011, 2018) and it is planned that new filters will be rebuilt for each GeoCarb release. For the experiments in this paper filters were built for baseline and it was determined that these filters ~~where were~~ sufficient for the radiometric calibration, ILS, polarization, and pointing experiments, although it was determined that new filters were required for the baseline with noise, spectroscopy, 10 meteorology, and kitchen sink experiments (a specific set of filters for each).

5.1.2 Bias Correction

Table 8 shows the bias correction parameters for the three target gases for the baseline experiment. ΔP explains the most variability in X_{CO_2} , followed by the AOT from large aerosols (dust, water cloud, and sea salt) as well as the fine mode aerosol (sulfate + organic carbon). These variables are all important in the operational OCO-2 X_{CO_2} bias correction (O’Dell et al., 2018), so their selection is not surprising. However, we see ΔP is also important for X_{CH_4} , but even more importantly is the retrieved ice cloud AOT, explaining 31% of the variance in retrieved X_{CH_4} . And, even though X_{CO} is mostly dominated by random error, the bias correction still reduces the systematic error from 0.8 to 0.5 ppb.

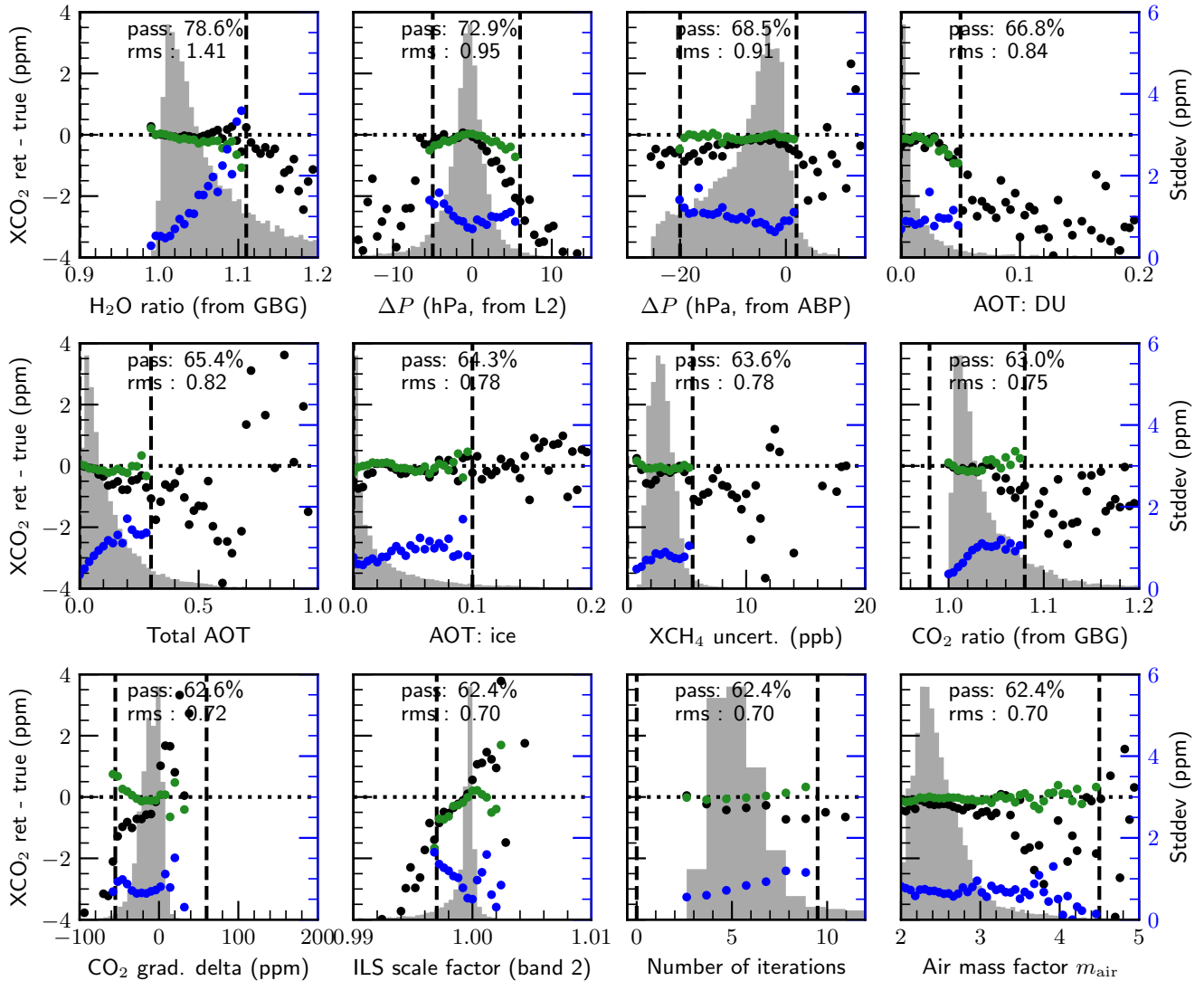


Figure 8. The top twelve most important filters in the post processing filtering algorithm applied cumulatively and sorted by importance from left-to-right and then from top-down. Background histograms show the distribution of the filter variable values, black dots show mean values of the difference between retrieved X_{CO_2} and true X_{CO_2} for each histogram bin (left axis), the blue dots show the standard deviation of the X_{CO_2} differences for each histogram bin (right axis), and the green dots show the mean X_{CO_2} differences for each bin after filtering and bias correction (left axis). The filter thresholds are shown as vertical dashed lines. The % of retrievals that pass the filter and RMS error of the results after the filter's application are also given for each variable.

5.1.3 Posterior Uncertainty

- 20 The ~~posterior~~ posterior estimate of uncertainty of X_{gas} for the baseline run (with aerosol/cloud and without noise added) is shown in figure ~~??~~ The 9. The ~~posterior~~ posterior uncertainty for X_{gas} is given by

$$\sigma_{X_{gas}} = \sqrt{\mathbf{h}^T \hat{\mathbf{S}}_{gas} \mathbf{h}}, \quad (21)$$

Table 7. Baseline filters applied cumulatively along with the thresholds and the % of retrievals that pass the filter and, for each gas, the mean error, standard deviation of the error, and the RMS error of X_{gas} after the filter's application. The units are in ppm, ppb, and ppb for X_{CO_2} , X_{CH_4} , and X_{CO} .

#	Name	Threshold	% pass	X_{CO_2}			X_{CH_4}			X_{CO}		
				μ	σ	RMS	μ	σ	RMS	μ	σ	RMS
	Raw, No BC			-0.35	2.48	2.51	16.47	27.41	31.97	-0.45	1.64	1.70
1	H ₂ O ratio (from GBG)	[0.90, 1.11]	78.59	-0.16	1.40	1.41	1.41	10.02	10.12	-0.02	0.96	0.96
2	ΔP (hPa, from L2)	[-5.00, 6.00]	72.89	-0.08	0.94	0.95	1.65	8.49	8.65	0.01	0.90	0.90
3	ΔP (hPa, from ABP)	[-20.00, 2.00]	68.46	-0.08	0.90	0.91	1.46	8.07	8.20	-0.01	0.86	0.86
4	AOT: DU	≤ 0.05	66.77	-0.05	0.84	0.84	1.47	8.05	8.19	-0.01	0.85	0.85
5	Total AOT	≤ 0.30	65.44	-0.06	0.81	0.82	1.33	7.81	7.92	-0.01	0.84	0.84
6	AOT: ice	≤ 0.10	64.29	-0.07	0.78	0.78	1.11	7.41	7.49	-0.03	0.81	0.81
7	XCH ₄ uncert. (ppb)	≤ 5.50	63.60	-0.07	0.77	0.78	1.01	7.05	7.12	-0.03	0.80	0.81
8	CO ₂ ratio (from GBG)	[0.98, 1.08]	62.99	-0.06	0.75	0.75	1.01	6.75	6.82	-0.02	0.79	0.79
9	CO ₂ grad. delta (ppm)	[-55.00, 60.00]	62.60	-0.06	0.72	0.72	1.04	6.68	6.76	-0.02	0.79	0.79
10	ILS scale factor (band 2)	[1.00, 2.00]	62.44	-0.05	0.70	0.70	1.06	6.63	6.71	-0.02	0.79	0.79
11	Number of iterations	≤ 9.50	62.38	-0.05	0.70	0.70	1.08	6.60	6.69	-0.02	0.79	0.79
12	Air mass factor m_{air}	≤ 4.50	62.35	-0.05	0.70	0.70	1.08	6.59	6.68	-0.02	0.79	0.79

where \hat{S}_{gas} is the portion of the ~~posteriori~~ posterior covariance matrix given by equation ?? that is for either the CO₂, CH₄, or CO retrieved profiles. ~~The posteriori estimate of X_{gas} error~~ While these error estimates should generally be a combination of instrument noise and forward model errors, ~~introduced in the $m \times m$ measurement and forward model error covariance matrix S_ϵ and the $n \times n$ a priori covariance matrix, along with smoothing error~~ for simplicity our input error estimates only include instrument noise, smoothing error (related to the prior covariance), and interference errors with unrelated state vector elements. ~~As mentioned already, for simplicity, S_ϵ is diagonal and populated only with uncorrelated channel variances while the forward model error is not considered. Forward model error includes not only RT assumptions, such as the plane-parallel assumption or discretization of layers and angles, but also assumptions about the elements of the vector of assumed parameters b . Not including forward model error is rather common in atmospheric retrieval methods due to the difficulty of quantifying the errors. Comparing the real errors and~~ Our posterior error estimates do not include forward model errors (such as that due to spectroscopy, aerosol assumptions, surface characterization, RT assumptions, etc.).

Figure 9 compares the RMS errors in the ~~estimated uncertainties in figures 6 and ??, respectively~~ retrieved gas column fractions with the estimated posterior uncertainty described above. Shown are the baseline case including bias correction (black), as well as the baseline with noise case with (blue) and without (red) bias correction. The grey histograms indicate the distribution of the posterior uncertainties for each gas. The mean posterior (i.e., noise-driven) uncertainties are 0.53 ppm,

Bias correction parameters:

Figure 4 shows the minimum, maximum, and mean normalized column averaging kernels for June 21, 2016 and December 21, 2016, respectively. The full averaging kernel matrix \mathbf{A} , given by equation ??, quantifies the response of the retrieval to changes in the true state vector about the retrieved state vector, which can be written as

$$\mathbf{A}_{i,j} = \frac{\partial \hat{x}_i}{\partial x_j}, i, j = 1, n,$$

where n is the number of state vector elements. The diagonal elements of \mathbf{A} range from zero to one, where for a perfect retrieval \mathbf{A} would be an identity matrix indicating that changes in each state vector element are perfectly represented by the retrieval. In the plots we show the normalized column averaging kernel \mathbf{a}_{gas} given by

$$\mathbf{a}_{\text{gas},j} = \frac{\partial X_{\text{gas}}}{\partial u_{\text{gas},j}} \frac{1}{h_j} = \left(\mathbf{h}^T \mathbf{A} \right)_j \frac{1}{h_j},$$

where j iterates through the portion of the state vector for the particular ‘gas’; u_{gas} is the true profile for CO_2 , CH_4 , or CO ; and h is the pressure weighting function. The column averaging kernel indicates the response of X_{gas} to changes in the true gas profile u_{gas} and, unlike the diagonal elements of \mathbf{A} , the values may be less than or greater than one. Again, for a perfect retrieval, with perfect sensitivity, the values would all be unity. From the figures it can be seen that the sensitivity to CO_2 and CH_4 is larger closer to the Earth’s surface. This is as expected and optimal since sensitivity to sources and sinks at the surface is an important requirement of the GeoCarb mission. On the other hand, there is generally an increase in sensitivity to CO with altitude as the mixing ratio of CO is larger higher up in the atmosphere.

Table 8. Normalized averaging kernels \mathbf{A}_N for X_{CO_2} , X_{CH_4} and X_{CO} for June 21 “ice” = ice crystals, 2016 (solid) and December 21 “DU” = desert dust, 2016 (dashed). Three averaging kernels are presented: one for the minimum geometric airmass factor m_{air} “SS” = sea salt, one for the maximum “SU” = sulfate, and one for the mean “OC” = organic carbon.

Parameter	Coefficient	% variance
XCO₂		
ΔP (hPa, from L2)	-0.22	29%
AOT: DU + wat + SS	-4.9	4.2%
AOT: SU + OC	11	9.4%
Total ($\sigma_{\text{raw}} = 0.87 \rightarrow \sigma_{\text{bc}} = 0.66$ ppm)		43%
XCH₄		
ΔP (hPa, from L2)	-1.7	17%
AOT: ice	270	31%
XCH ₄ uncert. (ppb)	3.1	6.2%
Airmass factor	4.2	2.3%
Total ($\sigma_{\text{raw}} = 9.2 \rightarrow \sigma_{\text{bc}} = 6.0$ ppb)		57%
XCO		
ILS scale factor (band 4)	272	37%
AOT: ice	17	15%
Total ($\sigma_{\text{raw}} = 0.79 \rightarrow \sigma_{\text{bc}} = 0.50$ ppb)		59%

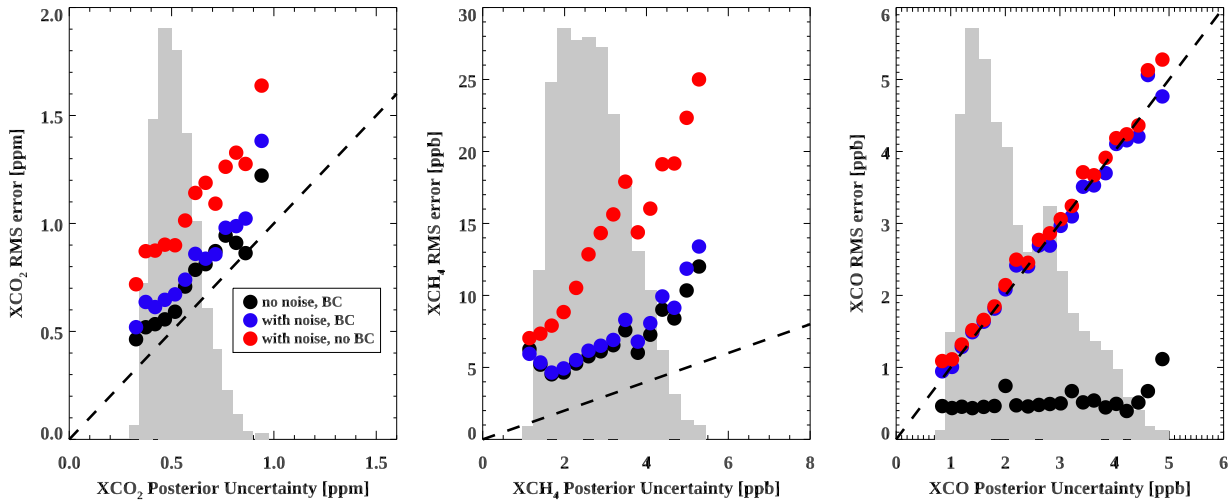


Figure 9. Baseline retrieval ~~estimated~~ actual errors in target gas column fractions plotted vs. the posterior uncertainty results. Shown are the noiseless errors with clouds and aerosols bias correction (all-sky black) for the unfiltered, with noise with bias correction (raw blue), and filtered cases with noise without bias correction (red).

2.7 ppb, and 2.2 ppb for X_{CO_2} , indicates underestimation of uncertainty for X_{CH_4} , and X_{CO} , respectively. As expected, there is an underestimation of the error for both X_{CO_2} and X_{CH_4} most likely due to the not including forward model errors, in particular that from spectroscopy and/or aerosol/clouds impact of systematic errors. This impact is largest for X_{CH_4} , indicating the importance of bias correction for that quantity. For X_{CO} (as well as SIF, see Somkuti et al., 2021), the uncertainties are more consistent with the actual errors, an indication that X_{CO} errors are driven less by systematic errors than X_{CO_2} and X_{CH_4}

, primarily due to less X_{CO} signal compared to the other gases. Relative to the noise-driven uncertainty, systematic errors in X_{CO} are almost negligible (less than 1 ppb).

5.2 Baseline with noise

15 The results when Gaussian noise is added to the baseline radiances are shown in figure 10. As already mentioned, a new filter was built specifically for this experiment. The results indicate that the accuracy-precision requirements are met by the filtered and bias corrected results with errors of -0.04 ± 0.76 ppm, 0.86 ± 6.89 RMS errors of 0.72 ppm, 6.4 ppb, and -0.13 ± 2.45 2.4 ppb for X_{CO_2} , X_{CH_4} , and X_{CO} , respectively. The filtering throughput of 7388 soundings (61%) is, as expected, slightly less than that for the baseline (7544 soundings). The addition of noise seems to have a relatively small impact on the filtered and
 20 bias corrected results for X_{CO_2} and X_{CH_4} indicating, 62%). These relatively small impacts of the synthetic noise indicate that the retrievals of X_{CO_2} and X_{CH_4} are driven primarily by systematic errors as we pointed out above. In contrast, the retrieval of

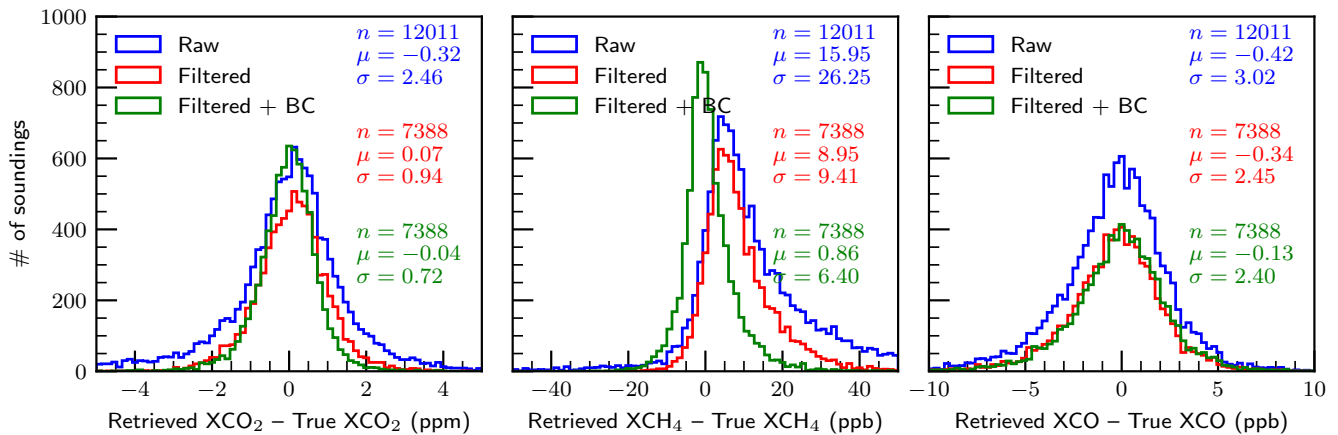


Figure 10. Same as figure 6 but with synthetic Gaussian noise added.

X_{CO} is significantly affected by the addition of noise supporting our previous observation that the X_{CO} retrieval is driven more by instrument noise. It is worth noting that in many applications the X_{gas} results will be averaged spatially and/or temporally in which case it is expected that the random error will decrease proportionally to \sqrt{n} where n is the number of soundings to be averaged.

5.3 Radiometric calibration

Results for the radiometric calibration perturbation experiment are shown in figure 11. In this experiment all channels were perturbed together by a scale factor of 1.05. From the figure it is apparent that even with the perturbation to the radiometric calibration the filtered and bias corrected X_{gas} results meet the ~~accuracy requirements with errors of -0.08 ± 0.70 ppm, 0.85 ± 6.68 ppb, and -0.01 ± 0.75 ppb~~ precision requirements with RMS errors of 0.64 ppm, 5.8 ppb, and 0.5 ppb for X_{CO_2} , X_{CH_4} , and X_{CO} , respectively, and a filter throughput of ~~7386 soundings~~ 7532 soundings (62%). ~~These results are very similar to the raw results of the baseline retrieval. The filter throughput of 7386 soundings is less than the 7544 of the baseline results, as expected, especially since they are using the same filter~~ baseline results, indicating that the retrieval is not particularly sensitive to an offset in the overall (multiplicative) radiometric calibration. As a test we performed this perturbation experiment with a 0.95 scale factor to make sure that the perturbation outcome is acceptably symmetric which the results (not shown) indicate. The results for each band perturbed individually (not shown), a total of four additional tests, show only a small improvement each compared to the results with all bands perturbed while compared to each other there is little noticeable differences between bands.

5.4 ILS

Results for the ILS perturbation experiment are shown in figure 12. The filtered and bias corrected results all fall within the ~~accuracy requirements with errors of -0.07 ± 0.70 ppm, 1.09 ± 6.78 ppb~~ precision requirements with RMS errors of 0.67 ppm, 6.3

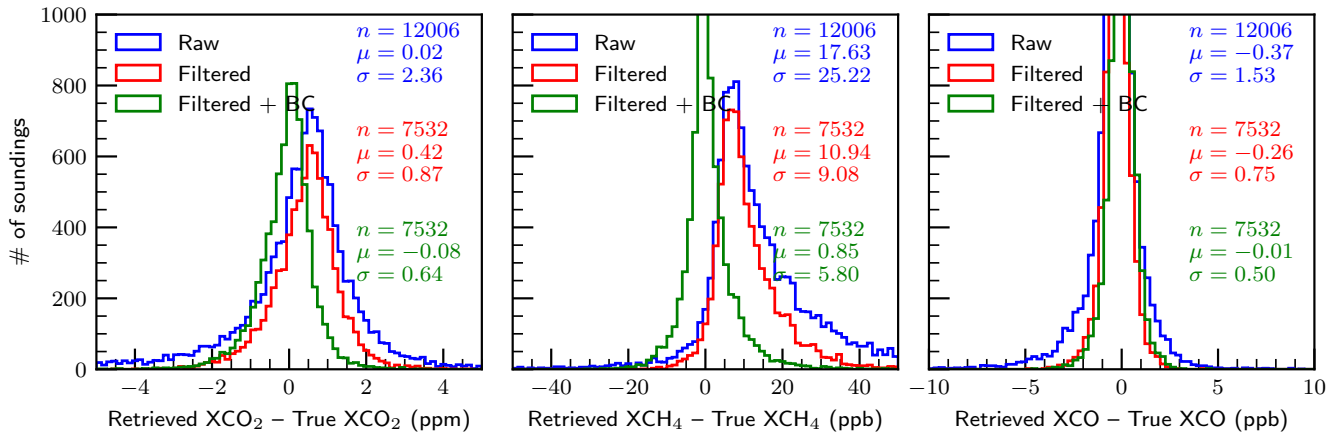


Figure 11. Same as figure 6 but for the case of imperfect knowledge of radiometric calibration for all bands.

ppb, and -0.00 ± 0.68 0.6 ppb for X_{CO_2} , X_{CH_4} , and X_{CO} , respectively, and a filter throughput of ~~7328 soundings~~ 7594 soundings (62%). Even the results that are not bias corrected meet the requirements. Again, perturbation symmetry was tested for this experiment with insignificant differences between perturbation directions. The results (with no bias correction) for each band perturbed individually (not shown) show a significantly larger bias in X_{CO_2} results for bands 2 and 3 compared to bands 1 and 4. Clearly this is an indication of the sensitivity to CO_2 in these bands relative to the others. There are three state vector parameters that ~~are fitted for that~~ affect these results: to a small degree the dispersion scale and offset and, more importantly, the ILS scaling which amounts to a total of twelve parameters, three for each band. As mentioned before, we specifically removed the ILS scale factor from the state vector for this test and as it turns out (results not shown) including the ILS scale factor in the state vector fits for the perturbation error down to a negligible error for X_{CO_2} and X_{CH_4} and just to a small error compared to the baseline run for X_{CO} , most likely due to the smaller sensitivity to X_{CO} compared to the other gases. Regardless, it is still instructive to apply this perturbation without the ILS scaling in the state vector, to show that the bias correction can still largely correct for this error. It is worth noting that the simulations for these experiments do not include scene inhomogeneity: ~~This subject is dedicated to two other papers that are currently in progress, which can strongly perturb the ILS. This effect is described in (Crowell et al., 2023).~~

5.5 Polarization

The results for the ~~experiment with no knowledge of polarization (by assuming that there is no polarization)~~ imperfect polarization experiment, wherein the retrievals assume the instrument is only sensitive to total intensity, when the simulations include a realistic polarization sensitivity, are shown in figure 13. The filtered and bias corrected results all fall within the requirements with errors of -0.05 ± 0.71 ppm, -1.02 ± 6.70 ppb precision requirements with RMS errors of 0.65 ppm, 6.0 ppb, and -0.01 ± 0.76 0.5 ppb for X_{CO_2} , X_{CH_4} , and X_{CO} , respectively, and a filter throughput of ~~7599 soundings~~ 7562 soundings (62%). The per-band results (not shown) indicate

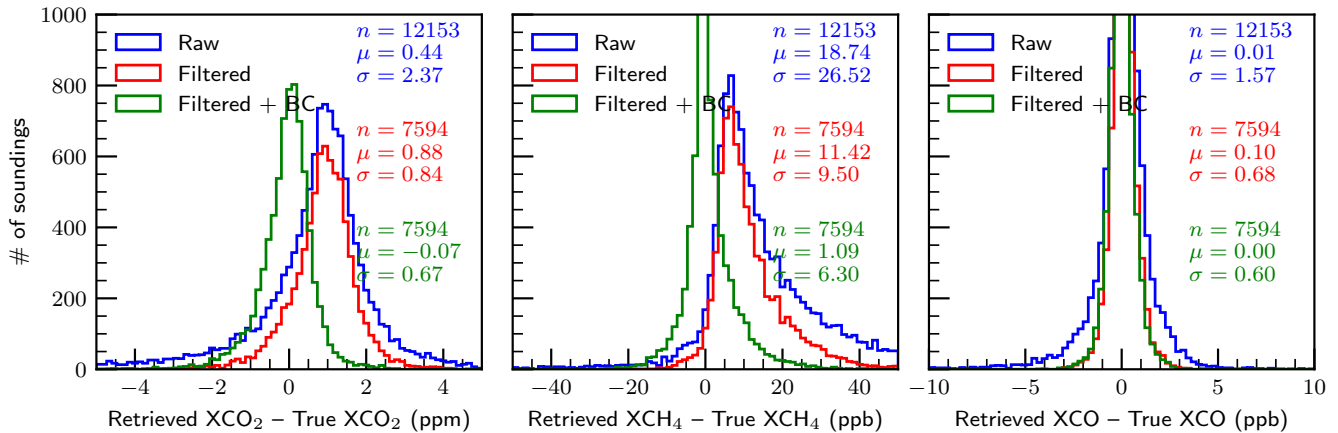


Figure 12. Same as figure 6 but with imperfect knowledge of the ILS.

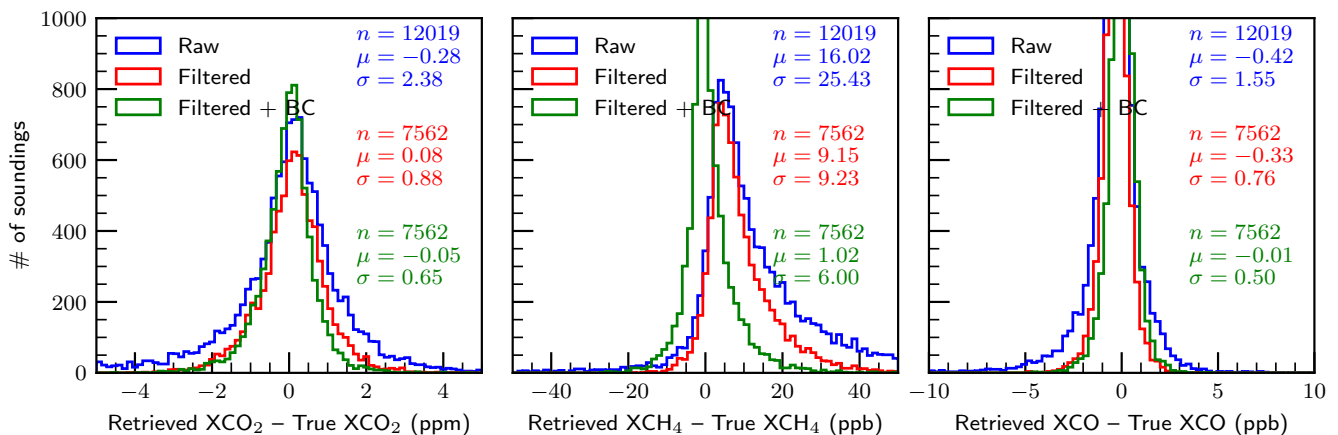


Figure 13. Same as figure 6 but with imperfect knowledge of polarization.

the that there is no significant distinction per band. [These findings are largely consistent with the earlier work in O2015, and indicate that a moderate knowledge of the instrument polarization response is sufficient to meet our requirements.](#)

5.6 Pointing

The results for the experiment with a perturbation in pointing are shown in figure 14. In this case we were limited to the single day of March 21, 2016 without the three other days. We believe in this experiment that this reduced dataset will have little impact on the results. For this case, the filtered and bias corrected results all fall within the [accuracy-precision requirements](#), and are actually very close to the corresponding baseline results, with [errors of \$-0.08 \pm 0.71\$ ppm, \$0.97 \pm 6.53\$ RMS errors of \$0.67\$ ppm, \$5.8\$ ppb, and \$-0.08 \pm 0.87\$ 0.5 ppb](#) for X_{CO_2} , X_{CH_4} , and X_{CO} , respectively. [Of course the filter throughput is](#)

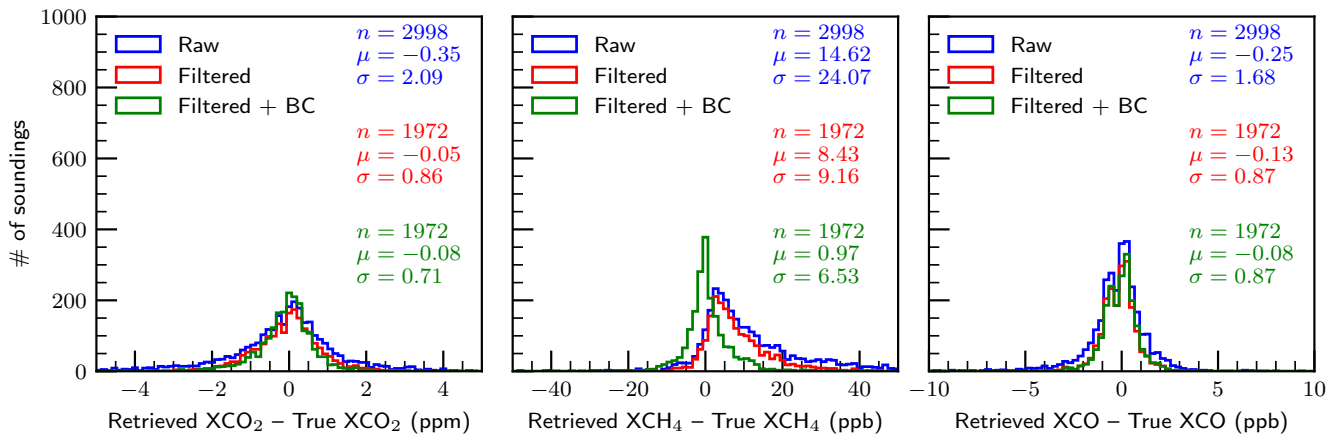


Figure 14. Same as figure 6 but with imperfect knowledge of the instrument pointing.

5 ~~less due to only using one day but, as approximation, multiplied by four it is 7869 soundings~~ The throughput fraction of 65% is marginally higher than that of the baseline (62%), likely due to this particular day having slightly less cloud contamination.

5.7 ~~Spectroscopy~~ Meteorology

The results for the ~~spectroscopy~~ meteorological perturbation experiment are shown in figure ~~16~~ 15. The filtered and bias corrected results ~~all fall within the accuracy requirements with errors of -0.02 ± 0.94 ppm, 0.65 ± 10.05~~ meet the precision requirements with RMS errors of 0.74 ppm, 6.5 ppb, and -0.11 ± 1.55 0.6 ppb for X_{CO_2} , X_{CH_4} , and X_{CO} , respectively.
~~As already mentioned, a new filter (not shown) was built for this experiment but this was~~ The errors are similar to baseline, although, with its own filter. This is at the cost of ~~significantly less filter throughput compared to baseline with only 5979 soundings passing with only 53% soundings passing the quality filter, versus 62% for the baseline.~~ Several parameters change significantly, in particular ΔP and $co2_grad_del$, which will affect the filtering. Finally, these filters were hand-tuned for
 15 simplicity, so some of the loss may simply be an imperfect filter.

5.8 ~~Meteorology~~ Spectroscopy

The results for the ~~meteorological~~ spectroscopy perturbation experiment are shown in figure ~~15~~ 16. The filtered and bias corrected results ~~meet the accuracy requirements with errors of -0.01 ± 0.90 ppm, 0.90 ± 7.27~~ all fall within the precision requirements with RMS errors of 0.84 ppm, 7.5 ppb, and -0.07 ± 1.06 0.6 ppb for X_{CO_2} , X_{CH_4} , and X_{CO} , respectively.
 20 ~~Even the case with no bias correction meets the requirements for X_{CO_2} and X_{CO} and comes close for X_{CH_4} . The errors are similar to baseline, although, with its own filter, this is~~ As already mentioned, a new filter (not shown) was built for this experiment but this was at the cost of ~~significantly less filter throughput with only 6630 soundings passing compared to baseline with only 6290 soundings passing (52%), similar to the meteorology perturbation experiment. Except for aerosols and clouds,~~

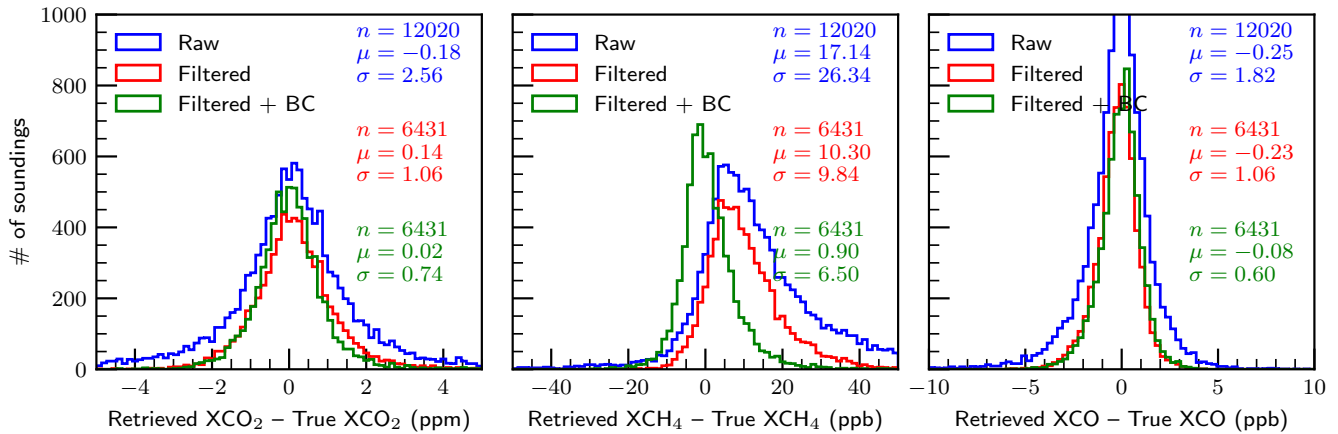


Figure 15. Same as figure 6 but with imperfect knowledge of [spectroscopy](#)[meteorology](#).

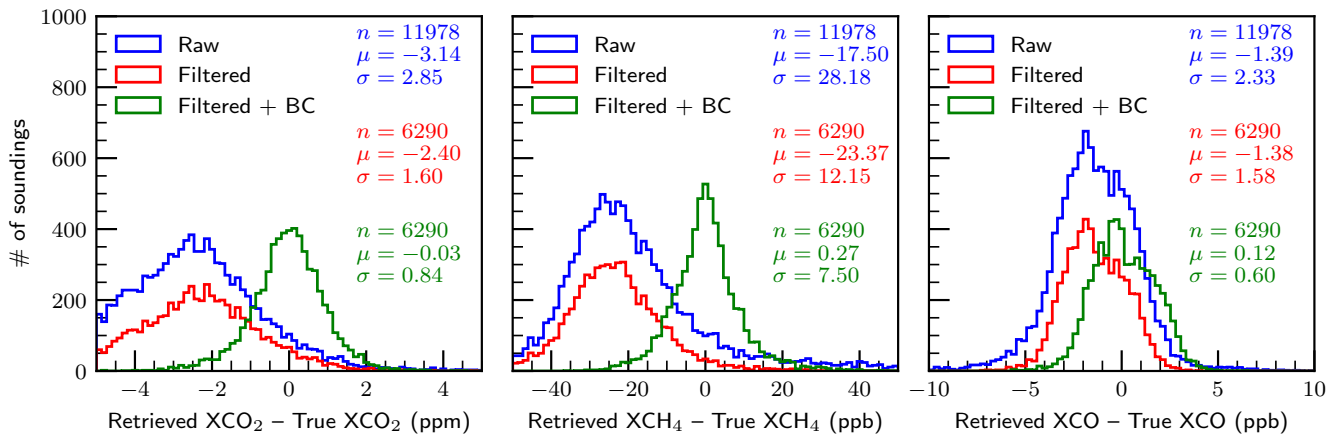


Figure 16. Same as figure 6 but with imperfect knowledge of [meteorology](#)[spectroscopy](#).

5 [error due to spectroscopy](#) represents the largest single systematic error source we studied in this work. This is consistent with [previous error analysis done for OCO-2 X_{CO₂} retrievals \(Connor et al., 2016; Hobbs et al., 2020\)](#).

5.9 Kitchen sink

The results for the kitchen sink experiment, [which simultaneously includes all the individually-discussed error sources above](#), are shown in figure 17. The errors for X_{CO₂} [do not quite meet the accuracy requirements although the results for X_{CH₄} and X_{CO} do, with errors of \$0.03 \pm 1.35\$ ppm, \$0.54 \pm 9.44\$ meet the precision requirements for all three target gases, with RMS errors of \$0.84\$ ppm, \$7.5\$ ppb, and \$-0.05 \pm 1.77\$ ppb for X_{CO₂}, X_{CH₄}, and X_{CO}, respectively. In addition, the same experiment was made with Gaussian noise added to the radiances. \[All three target gas species still meet our mission requirements after filtering\]\(#\)](#)

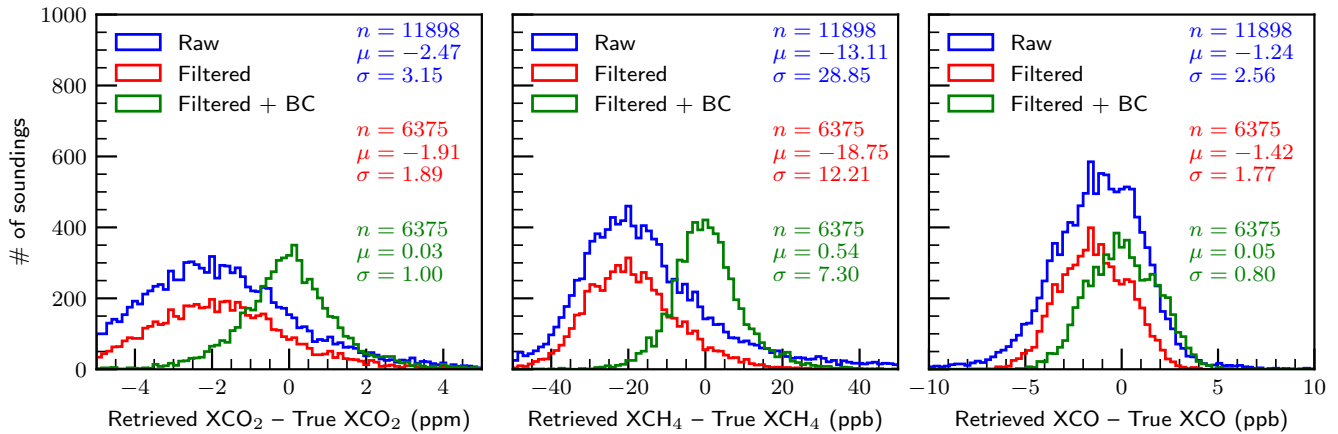


Figure 17. Same as figure 6 but for the 'kitchen sink' experiment.

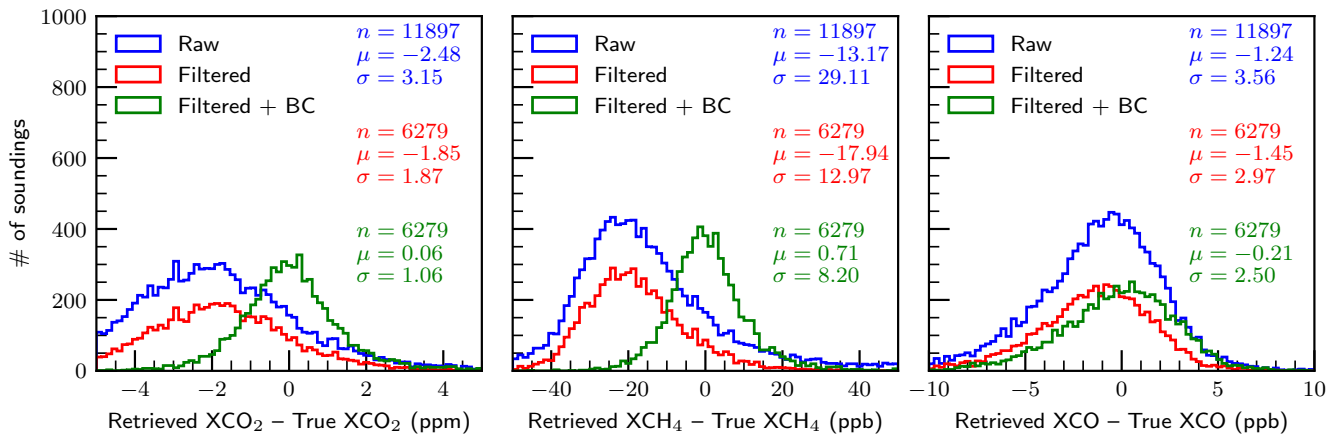


Figure 18. Same as figure 6 but for the 'kitchen sink' with noise experiment.

and bias correction. The results from X_{CO_2} and X_{CH_4} are similar to those from radiances without noise ~~although X_{CH_4} does not quite meet the accuracy requirements~~, while the largest effect of adding noise was for X_{CO} . ~~This is X_{CO} . The quadratic differences of these is another estimate of the pure noise-driven error or precision of our measurements, which are roughly 0.3 ppm, 3.6 ppb, and 2.3 ppb for X_{CO_2} , X_{CH_4} , and X_{CO} , respectively. These values are roughly~~ consistent with results from the baseline experiment with noise added. The ~~filter throughput with the special kitchen sink filters is 6095 and 5993 for with and without noise added, respectively. This fraction passing the quality filter, 53% without noise and 52% with noise,~~ is significantly less than baseline and is primarily driven by the spectroscopy and meteorological errors.

5.10 Error budget

In tables ?? and ?? error budgets are provided for the filtered case with no bias correction and for the case with a bias correction, respectively. Table 9 attempts to provide an approximate overall error budget for the target gases analyzed here. The errors are for filtered and bias-corrected results. The error for each experiment is listed including the total error for each X_{gas} (standard deviation σ given in the corresponding error histograms) and the component error, i.e. the error caused by the experiment's perturbation alone relative to baseline. The only bias corrected cases that don't meet the mission error requirements are X_{CO_2} in both kitchen sink experiments and X_{CH_4} in the kitchen sink with noise experiment. Component errors were calculated by assuming they are independent of the systematic errors in the baseline "with aerosols & clouds (a/c)" run, which thus add in quadrature. So for component j

$$X_{\text{gas},j} = \sqrt{X_{\text{gas},j}^2 - X_{\text{a/c}}^2}. \quad (22)$$

All experiments pass our precision and accuracy requirements given in table 1. The component errors for the spectroscopy and meteorology experiments are relatively large and this propagates into the kitchen sink experiments. These errors are estimates only, and do not always add quadratically when combined. These errors are therefore only best-guesses based upon the assumptions we've made. The dominant sources of systematic errors are, unsurprisingly, aerosols and clouds, meteorological errors, and spectroscopic errors. X_{CO} errors are dominated by random noise, while X_{CO_2} and X_{CH_4} are dominated by systematic errors. We can see that with perfect spectroscopy, typically 62% of soundings pass the quality filters over land, but spectroscopic errors reduce this to $\sim 52\%$. For X_{CO_2} , these results are surprisingly consistent with baseline errors and fractions seen by OCO-2 (O'Dell et al., 2018; Kiel et al., 2019).

6 Conclusions

The goal of this paper is to describe the GeoCarb L2FP algorithm and to present a study of the sensitivity of L2FP and the retrieved X_{CO_2} , X_{CH_4} , and X_{CO} to sources of uncertainty in several perturbation experiments using measurements simulated with the CSU L1B simulator. A description of the GeoCarb mission is given and details of the L2FP algorithm are discussed. A description of the experimental dataset including the scan strategy is presented, the CSU simulator is described, and the individual experiments were described. The results were presented and discussed and, finally, an error budget was presented in tabular form.

There are several key points that can be taken away from this study which are listed below:

- Retrievals of X_{CO_2} and X_{CH_4} errors of X_{CO_2} and X_{CH_4} are driven primarily by systematic errors.
- Retrievals of X_{CO} errors of X_{CO} are primarily driven by random error, though these errors (~ 2.5 ppb) are much smaller than the mission requirement of 12 ppb, suggesting GeoCarb will do better than expected with this important gas.
- With the addition of Gaussian noise to the radiances of the baseline experiment the filtered and bias corrected results still meet the requirements. Retrievals of X_{CO_2} , X_{CH_4} , and X_{CO} meet the mission precision requirements for all error sources, alone and in combination.

Table 9. Final error budget for each experiment ~~without the bias correction, filtered and bias-corrected,~~ including the total error and the component error (the error caused by the experiment’s perturbation alone). N_{proc} is the number of soundings processed after pre-screening, N_{conv} is the number of soundings that converged, and N_{good} is the number of soundings that passed the filtering.

~~Same as table ?? but including the bias correction.~~

Run Name	Total Error			Component Error			$N_{\text{conv}} / N_{\text{proc}}$	N_{good} (%)
	XCO ₂	XCH ₄	XCO	XCO ₂	XCH ₄	XCO		
	ppm	ppb	pbb	ppm	ppb	ppb		
With aerosols and clouds (a/c)	0.66	6.0	0.5	0.66	6.0	0.5	12018 / 12101	7544 (62%)
W. a/c, with noise	0.72	6.4	2.4	0.29	2.2	2.3	12011 / 12096	7388 (61%)
W. a/c, pert. rad. cal.	0.64	5.8	0.5	0	0	0	12006 / 12086	7532 (62%)
W. a/c, pert. ILS	0.67	6.3	0.6	0.1	2.0	0.4	12153 / 12246	7594 (62%)
W. a/c, pert. polarization	0.65	6.0	0.5	0	0	0	12019 / 12106	7562 (62%)
W. a/c, pert. pointing	0.67	5.8	0.5	0.1	0	0.1	3000 / 3016	1972 (65%)
W. a/c, pert. meteorology	0.74	6.5	0.6	0.35	2.4	0.3	12020 / 12110	6431 (53%)
W. a/c, pert. spectroscopy	0.84	7.5	0.6	0.53	4.4	0.4	11978 / 12119	6290 (52%)
W. a/c, pert. kit. sink	1.00	7.3	0.8	-	-	-	11898 / 12040	6375 (53%)
W. a/c, pert. kit. sink, with noise	1.06	8.2	2.5	-	-	-	11897 / 12040	6279 (52%)

- Aerosols and spectroscopy form the majority of the systematic errors for all three gases.
- 30 - EOFs haven’t been included, and it is unclear what their effects will be, especially for the spectroscopy perturbation.
- ~~The retrieval of XCO₂ meets the requirements in the meteorology and spectroscopy experiments but it is apparent that applying both perturbations in the kitchen sink experiment pushes the accuracy passed the requirements. This is also the case for XCH₄ when noise is added.~~
- ~~The spectroscopy and meteorological experiments are a bit problematic due to the number of soundings spectroscopic error experiments cause an additional ~ 10% of soundings to be filtered out. It is possible that the perturbation in spectroscopy is not representative of reality or maybe that EOFs are required.~~
- 5 Aerosols and spectroscopy form the majority of the systematic errors for all three gases by including EOFs in the retrieval, this effect could be mitigated.
- The calibration related errors (radiometric gain, ILS, and polarization) do not account for a significant portion of the error in the results, but the calibration errors are not exhaustive. As mentioned before, this study does not account for instrument affects other instrument effects such as smile, keystone, stray light, gain nonlinearity, and detector persistence. In addition, the effects of scene inhomogeneity are also not taken into account and therefore ILS variation across the
- 5 scene is ignored. These effects could end up being significant and will be treated in forthcoming papers.

- ~~There is very little difference in the errors for radiometric gain, ILS, and polarization when the perturbations are applied per-band compared to applying them for all bands at the same time. This needs to be investigated. For example, is there a cancellation between bands in the case of all bands?~~
- The filtering was trained for X_{CO_2} - X_{CO_2} for simplicity although, given the larger errors for X_{CH_4} - X_{CH_4} it will most likely require more filtering and ~~there for it's~~ therefore its own filter. In contrast, X_{CO} - X_{CO} will require less filtering. This will be addressed as the GeoCarb L2FP product is improved over time.

There are several in progress or planned next-steps related to this study. As the instrument model develops retrieval simulations will have to take into account the instrument ~~affects~~effects, such as the ~~optical aberrations mentioned above~~effects of scene inhomogeneity and the other effects mentioned previously, that are ignored in this study. This will require modifications to the CSU simulator and the L2FP code. In addition, EOFs will be produced, and their ~~affects~~effects on the retrieval investigated. Finally, modifications to the filtering process to fine tune the filtering for each gas separately are also planned. These next-steps are ongoing or planned and will be addressed in subsequent papers.

Code availability. The GeoCarb L2FP algorithm code is available at: <https://github.com/GeoCarb/RtRetrievalFramework>

Author contributions. GM wrote the manuscript, adapted and maintained the full-physics retrieval code for GeoCarb, ran all the tests, and performed data analysis. CO helped conceive the idea, generated synthetic scenes on which to run experiments, performed data analysis and interpretation, and edited the text. SC helped with experimental set-up and interpretation of results. PS wrote the GASBAG code and reviewed the text. EB provided the instrument model and instrument perturbation parameters.

Competing interests. The authors declare no competing interests.

Acknowledgements. ~~Acknowledge Joshua Laughner for the description of the trace gas a priori.~~ Josh Laughner at JPL provided the TCCON trace gas prior code. This work was funded by NASA through the GeoCarb Mission under award 80LARC17C0001.

References

- Baker, D. F., Bösch, H., Doney, S. C., O'Brien, D., and Schimel, D. S.: Carbon Source/sink Information Provided by Column CO₂ Measurements from the Orbiting Carbon Observatory, *Atmos. Chem. and Phys.*, 10, 4145–4165, <https://doi.org/10.5194/acp-10-4145-2010>, 2010.
- 30 Barkley, M. P., Frie, U., and Monks, P. S.: Measuring Atmospheric CO₂ from Space Using Full Spectral Initiation (FSI) WFM-DOAS, *Atmos. Chem. and Phys.*, 6, 3517–3534, <https://doi.org/10.5194/acp-6-3517-2006>, 2006.
- Baum, B. A., Yang, P., Heymsfield, A. J., Bansemer, A., Cole, B. H., Merrelli, A., Schmitt, C., and Wang, C.: Ice Cloud Single-Scattering Property Models with the Full Phase Matrix at Wavelengths from 0.2 to 100 μm , *J. Quant. Spectrosc. Radiat. Transfer.*, 146, 123–139, <https://doi.org/10.1016/j.jqsrt.2014.02.029>, 2014.
- 35 Bergamaschi, P., Hein, R., Heimann, M., and Crutzen, P. J.: Inverse Modeling of the Global CO Cycle: 1. Inversion of CO Mixing Ratios, *J. Geophys. Res.*, 105, 1909–1927, <https://doi.org/10.1029/1999JD900818>, 2000.
- Bergamaschi, P., Frankenberg, C., Meirink, J. F., Krol, M., Villani, M. G., Houweling, S., Dentener, F., Dlugokencky, E. J., Miller, J. B., Gatti, L. V., Engel, A., and Levin, I.: Inverse Modeling of Global and Regional CH₄ Emissions Using SCIAMACHY Satellite Retrievals, *J. Geophys. Res.*, 114, D22301, <https://doi.org/10.1029/2009JD012287>, 2009.
- 5 Bovensmann, H., Burrows, J. P., Buchwitz, M., Frerick, J., Noël, S., and Rozanov, V. V.: SCIAMACHY: Mission Objectives and Measurement Modes, *J. Atmos. Sci.*, 56, 127–150, [https://doi.org/10.1175/1520-0469\(1999\)056<0127:SMOAMM>2.0.CO;2](https://doi.org/10.1175/1520-0469(1999)056<0127:SMOAMM>2.0.CO;2), 1999.
- Bril, A., Oshchepkov, S., Yokota, T., and Inoue, G.: Parameterization of Aerosol and Cirrus Cloud Effects on Reflected Sunlight Spectra Measured from Space: Application of the Equivalence Theorem, *Appl. Opt.*, 46, 2460–2470, <https://doi.org/10.1364/AO.46.002460>, 2007.
- Buchwitz, M., Rozanov, V. V., and Burrows, J. P.: A Near-infrared Optimized DOAS Method for the Fast Global Retrieval of Atmospheric
- 10 CH₄, CO, CO₂, H₂O, and N₂O Total Column Amounts from SCIAMACHY Envisat-1 Nadir Radiances, *J. Geophys. Res.*, 105, 15 231–15 245, <https://doi.org/10.1029/2000JD900191>, 2000.
- Buchwitz, M., de Beek, R., Noël, S., Burrows, J. P., Bovensmann, H., Bergamaschi, H. B. P., Körner, S., and Heimann, M.: Carbon Monoxide, Methane and Carbon Dioxide Columns Retrieved from SCIAMACHY by WFM-DOAS: Year 2003 Initial Data Set, *Atmos. Chem. and Phys.*, 5, 3313–3329, <https://doi.org/10.5194/acp-5-3313-2005>, 2005.
- 15 Buchwitz, M., de Beek, R., Noël, S., Burrows, J. P., Bovensmann, H., Schneising, O., Khlystova, I., Bruns, M., Bremer, H., Bergamaschi, P., Körner, S., and Heimann, M.: Atmospheric Carbon Gases Retrieved from SCIAMACHY by WFM-DOAS: Version 0.5 CO and CH₄ and Impact of Calibration Improvements on CO₂ Retrieval, *Atmos. Chem. and Phys.*, 6, 2727–2751, <https://doi.org/10.5194/acp-6-2727-2006>, 2006.
- Buchwitz, M., Reuter, M., Schneising, O., Hewson, W., Detmers, R., Boesch, H., Hasekamp, O., Aben, I., Bovensmann, H., Burrows, J., Butz, A., Chevallier, F., Dils, B., Frankenberg, C., Heymann, J., Lichtenberg, G., De Mazière, M., Notholt, J., Parker, R., Warneke, T., Zehner, C., Griffith, D., Deutscher, N., Kuze, A., Suto, H., and Wunch, D.: Global Satellite Observations of Column-averaged Carbon Dioxide and Methane: The GHG-CCI XCO₂ and XCH₄ CRDP3 Data Set, *Remote Sens. Environ.*, 203, 276–295, <https://doi.org/10.1016/j.rse.2016.12.027>, 2017.
- 20 Butz, A., Hasekamp, O. P., Frankenberg, C., and Aben, I.: Retrievals of Atmospheric CO₂ from Simulated Space-borne Measurements of Backscattered Near-infrared Sunlight: Accounting for Aerosol Effects, *Appl. Opt.*, 48, 3322–3336, 2009.
- 25

- Butz, A., Hasekamp, O. P., Frankenberg, C., Vidot, J., and Aben, I.: CH₄ Retrievals from Space-based Solar Backscatter Measurements: Performance Evaluation Against Simulated Aerosol and Cirrus Loaded Scenes, *J. Geophys. Res.*, 115, D24302, <https://doi.org/10.1029/2010JD014514>, 2010.
- Chevallier, F., Engelen, R. J., and Peylin, P.: The Contribution of AIRS Data to the Estimation of CO₂ Sources and Sinks, *Geophys. Res. Lett.*, 32, 1–4, <https://doi.org/10.1029/2005GL024229>, 2005.
- Connor, B., Bösch, H., McDuffie, J., Taylor, T., Fu, D., Frankenberg, C., O'Dell, C., Gunson, V. H. P. M., Hobbs, R. P. J., Oyafuso, F., and Jiang, Y.: Quantification of Uncertainties in OCO-2 Measurements of XCO₂: Simulations and Linear Error Analysis, *Atmos. Meas. Tech.*, 9, 5227–5238, <https://doi.org/10.5194/amt-9-5227-2016>, 2016.
- Connor, B. J., Boesch, H., Toon, G., Sen, B., Miller, C., and Crisp, D.: Orbiting Carbon Observatory: Inverse Method and Prospective Error Analysis, *J. Geophys. Res.*, 113, D05305, <https://doi.org/10.1029/2006JD008336>, 2008.
- Crisp, D., Atlas, R. M., Breon, F.-M., Brown, L. R., Burrows, J. P., Ciais, P., Connor, B. J., Doney, S. C., Fung, I. Y., Jacob, D. J., Miller, C. E., O'Brien, D., Pawson, S., Randerson, J. T., Rayner, P., Salawitch, R. J., Sander, S. P., Sen, B., Stephens, G. L., Tans, P. P., Toon, G. C., Wennberg, P. O., et al.: The Orbiting Carbon Observatory (OCO) mission, *Adv. Space. Res.*, 34, 700–709, <https://doi.org/10.1016/j.asr.2003.08.062>, 2004.
- Crisp, D., Fisher, B. M., O'Dell, C., Frankenberg, C., Basilio, R., Bösch, H., Brown, L. R., Castano, R., Connor, B., Deutscher, N. M., Eldering, A., Griffith, D., Gunson, M., Kuze, A., Mandrake, L., McDuffie, J., Messerschmidt, J., Miller, C. E., Morino, I., Natraj, V., Notholt, J., O'Brien, D. M., Oyafuso, F., Polonsky, I., Robinson, J., Salawitch, R., Sherlock, V., Smyth, M., Suto, H., Taylor, T. E., Thompson, D. R., Wennberg, P. O., Wunch, D., and Yung, Y. L.: The ACOS CO₂ Retrieval Algorithm - Part II: Global X_{CO₂} data characterization, *Atmos. Meas. Tech.*, 5, 687–707, <https://doi.org/10.5194/amt-5-687-2012>, 2012.
- Crowell, S., Haist, T., Tscherpel, M., Caron, J., Burgh, E., and Moore III, B.: Performance and Polarization Response of Slit Homogenizers for the GeoCarb Mission, *Atmos. Meas. Tech.*, 16, 195–208, <https://doi.org/10.5194/amt-16-195-2023>, 2023.
- Crowell, S. M. R., Kawa, S. R., Browell, E. V., Hammerling, D. M., Moore, B., Schaefer, K., and Doney, S. C.: On the Ability of Space-Based Passive and Active Remote Sensing Observations of CO₂ to Detect Flux Perturbations to the Carbon Cycle, *J. Geophys. Res.*, 123, 1460–1477, <https://doi.org/10.1002/2017JD027836>, 2018.
- Crutzen, P.: A Discussion of the Chemistry of Some Minor Constituents in the Stratosphere and Troposphere, *Photochemistry*, 106–108, 1385–1399, <https://doi.org/10.1007/BF00881092>, 1973.
- Deeter, M. N., Emmons, L. K., Francis, G. L., Edwards, D. P., Gille, J. C., Warner, J. X., Khattatov, B., Ziskin, D., Lamarque, J. F., Ho, S. P., Yudin, V., Attié, J. L., Packman, D., Chen, J., Mao, D., and Drummond, J. R.: Operational Carbon Monoxide Retrieval Algorithm and Selected Results for the MOPITT Instrument, *J. Geophys. Res.*, 108, 4399, <https://doi.org/10.1029/2002JD003186>, 2003.
- Deeter, M. N., Emmons, L. K., Edwards, D. P., and Gille, J. C.: Vertical Resolution and Information Content of CO Profiles Retrieved by MOPITT, *Geophys. Res. Lett.*, 31, L15112, <https://doi.org/10.1029/2004GL020235>, 2004.
- Doicu, A., Trautmann, T., and Schreier, F.: Numerical Regularization for Atmospheric Inverse Problems, Springer Praxis Books, Springer Berlin Heidelberg, <https://doi.org/10.1007/978-3-642-05439-6>, 2010.
- Edwards, D. P., Emmons, L. K., Hauglustaine, D. A., Chu, D. A., Gille, J. C., Kaufman, Y. J., Petron, G., Yurganov, L. N., Giglio, L., Deeter, M. N., Yudin, V., Ziskin, D. C., Warner, J., Lamarque, J. F., Francis, G. L., Ho, S. P., Mao, D., Chen, J., Grechko, E. I., and Drummond, J. R.: Observations of Carbon Monoxide and Aerosols from the Terra Satellite: Northern Hemisphere Variability, *J. Geophys. Res.*, 109, D24202, <https://doi.org/10.1029/2004JD004727>, 2004.

- Eldering, A., Taylor, T. E., O'Dell, C. W., and Pavlick, R.: The OCO-3 Mission: Measurement Objectives and Expected Performance Based on 1 Year of Simulated Data, *Atmos. Meas. Tech.*, 12, 2341–2370, <https://doi.org/10.5194/amt-12-2341-2019>, 2019.
- Frankenberg, C., Platt, U., and Wagner, T.: Iterative Maximum a Posteriori (IMAP)-DOAS for Retrieval of Strongly Absorbing Trace Gases: Model Studies for CH₄ and CO₂ Retrieval from Near-infrared Spectra of SCIAMACHY Onboard ENVISAT, *Atmos. Chem. and Phys.*, 5, 9–22, <https://doi.org/10.5194/acp-5-9-2005>, 2005.
- 30 Frankenberg, C., O'Dell, C., Berry, J., Guanter, L., Joiner, J., Köhler, P., Pollock, R., and E. Taylor, T.: Prospects for Chlorophyll Fluorescence Remote Sensing from the Orbiting Carbon Observatory-2, *Remote Sens. Environ.*, 147, 1–12, <https://doi.org/10.1016/j.rse.2014.02.007>, 2014.
- GeoCarb MDRA: GeoCarb Mission Definition Requirements Agreement, Tech. Rep. GEOCARB-SYS-REQ-0004 Rev. C, Lockheed Martin Space System Company, Advanced Technology Center – CAGE 65113, Lockheed Martin Solar & Astrophysics Laboratory (LMSAL), 3251 Hanover Street, Palo Alto, CA 94304-1191, 2020.
- 35 Granier, C., Müller, J., Pétron, G., and Brasseur, G.: A Three-dimensional Study of the Global CO Budget, *Chemosphere*, 1, 255–261, [https://doi.org/10.1016/S1465-9972\(99\)00007-0](https://doi.org/10.1016/S1465-9972(99)00007-0), 1999.
- Gurney, K. R., Law, R. M., Denning, A. S., Rayner, P. J., Baker, D., Bousquet, P., Bruhwiler, L., Chen, Y.-H., Ciais, P., Fan, S., Fung, I. Y., Gloor, M., Heimann, M., Higuchi, K., John, J., Kowalczyk, E., Maki, T., Maksyutov, S., Peylin, P., Prather, M., Pak, B. C., Sarmiento, J., Taguchi, S., Takahashi, T., and Yuen, C.-W.: TransCom 3 CO₂ inversion intercomparison: 1. Annual mean control results and sensitivity to transport and prior flux information, *Tellus*, 55B, 555–579, <https://doi.org/10.3402/tellusb.v55i2.16728>, 2003.
- 5 Hakkarainen, J., Ialongo, I., and Tamminen, J.: Direct Space-based Observations of Anthropogenic CO₂ Emission Areas from OCO-2, *Geophys. Res. Lett.*, 43, 11 400–11 406, <https://doi.org/10.1002/2016GL070885>, 2016.
- Hansen, J. E.: Multiple Scattering of Polarized Light in Planetary Atmospheres. Part I. The Doubling Method, *J. Atmos. Sci.*, 28, 120–124, [https://doi.org/10.1175/1520-0469\(1971\)028<1400:MSOPLI>2.0.CO;2](https://doi.org/10.1175/1520-0469(1971)028<1400:MSOPLI>2.0.CO;2), 1971.
- Hobbs, J. M., Drouin, B. J., Oyafuso, F., Payne, V. H., Gunson, M. R., McDuffie, J., and Mlawer, E. J.: Spectroscopic Uncertainty Impacts on OCO-2/3 Retrievals of XCO₂, *J. Quant. Spectrosc. Radiat. Transfer.*, 257, 107 360, <https://doi.org/10.1016/j.jqsrt.2020.107360>, 2020.
- 10 Hu, H., Hasekamp, O., Butz, A., Galli, A., Landgraf, J., de Brugh, J. A., Borsdorff, T., Scheepmaker, R., and Aben, I.: The Operational Methane Retrieval Algorithm for TROPOMI, *Atmos. Meas. Tech.*, 9, 5423–5440, <https://doi.org/10.5194/amt-9-5423-2016>, 2016.
- Intergovernmental Panel on Climate Change (IPCC): Climate Change 2013 - The Physical Science Basis: Working Group I Contribution to the Fifth Assessment Report of the IPCC, Tech. rep., Cambridge, UK, 2013.
- 15 Intergovernmental Panel on Climate Change (IPCC): Climate Change 2021: The Physical Science Basis. Contribution of Working Group I to the Sixth Assessment Report of the IPCC, Tech. rep., Cambridge, UK, 2021.
- Irizar, J., Melf, M., Bartsch, P., Koehler, J., Weiss, S., Greinacher, R., Erdmann, M., Kirschner, V., Albinana, A. P., and Martin, D.: Sentinel-5/UVNS, in: International Conference on Space Optics — ICSO 2018, edited by Sodnik, Z., Karafolas, N., and Cugny, B., vol. 11180, p. 1118004, International Society for Optics and Photonics, SPIE, <https://doi.org/10.1117/12.2535923>, 2019.
- 20 Jacob, D. J., Turner, A. J., Maasakkers, J. D., Sheng, J., Sun, K., Liu, X., Chance, K., Aben, I., McKeever, J., and Frankenberg, C.: Satellite Observations of Atmospheric Methane and their Value for Quantifying Methane Emissions, *Atmos. Chem. and Phys.*, 16, 14 371–14 396, <https://doi.org/10.5194/acp-16-14371-2016>, 2016.
- Joiner, J., Yoshida, Y., Vasilkov, A. P., Middleton, E. M., Campbell, P. K. E., Yoshida, Y., A., A. K. L., and Corp: Filling-in of Near-infrared Solar Lines by Terrestrial Fluorescence and other Geophysical Effects: Simulations and Space-based Observations from SCIAMACHY and GOSAT, *Atmos. Meas. Tech.*, 5, 809–829, <https://doi.org/10.5194/amt-5-809-2012>, 2012.
- 25

- Kanakidou, M. and Crutzen, P. J.: The Photochemical Source of Carbon Monoxide: Importance, Uncertainties and Feedbacks, *Chemosphere*, 1, 91–109, [https://doi.org/10.1016/S1465-9972\(99\)00022-7](https://doi.org/10.1016/S1465-9972(99)00022-7), 1999.
- Keely, W., Crowell, S., Moore, B., Diochnos, D., and O’Dell, C.: Geophysical Bias Correction of Trace Green House Gas Satellite Retrievals Using Explainable Machine Learning Methods, in: AGU Fall Meeting Abstracts, pp. A55R–1656, American Geophysical Union (AGU), American Geophysical Union (AGU), New Orleans, LA, 2021.
- 30 Kiel, M., O’Dell, C. W., Fisher, B., Eldering, A., Nassar, R., MacDonald, C. G., and Wennberg, P. O.: How Bias Correction Goes Wrong: Measurement of X_{CO_2} Affected by Erroneous Surface Pressure Estimates, *Atmos. Meas. Tech.*, 12, 2241–2259, <https://doi.org/10.5194/amt-12-2241-2019>, 2019.
- Kumer, J., Rairden, R., and Roche, A.: Modeling the 2.33 μm TIMS spectrometer radiometric noise: Implications for space applications, in: 2013 IEEE Aerospace Conference, pp. 1–20, <https://doi.org/10.1109/AERO.2013.6497369>, 2013.
- 35 Kumer, J. B., Roche, A. E., Rairden, R. L., Desouza-Machado, S., Blatherwick, R., Hawat, T., and Chatfield, R.: NASA ESTO IIP Tropospheric Infrared Mapping Spectrometers (TIMS) demonstration of multi-layer CO retrieval from atmospheric data acquired simultaneously in the solar reflective region near 2330 nm and the thermal emissive region near 4680 nm, in: *Advances in Imaging*, p. HMC5, Optical Society of America, <https://doi.org/10.1364/HISENSE.2009.HMC5>, 2009.
- Kumer, J. J. B., Rairden, R. L., Roche, A. E., and Chatfield, R.: NASA ESTO IIP Tropospheric Infrared Mapping Spectrometers (TIMS) Demonstration First Deployment on an Airship: Preliminary Results, in: *Imaging and Applied Optics*, p. HTuD2, Optical Society of America, <https://doi.org/10.1364/HISE.2011.HTuD2>, 2011.
- 5 Kuze, A., Suto, H., Nakajima, M., and Hamazaki, T.: Thermal and Near Infrared Sensor for Carbon Observation Fourier-Transform Spectrometer on the Greenhouse Gases Observing Satellite for Greenhouse Gases Monitoring, *Appl. Opt.*, 48, 6716–6733, <https://doi.org/10.1364/AO.48.006716>, 2009.
- Landgraf, J., aan de Brugh, J., Scheepmaker, R., Borsdorff, T., Hu, H., Houweling, S., Butz, A., Aben, I., and Hasekamp, O.: Carbon Monoxide Total Column Retrievals from TROPOMI Shortwave Infrared Measurements, *Atmos. Meas. Tech.*, 9, 4955–4975, <https://doi.org/10.5194/amt-9-4955-2016>, 2016.
- 10 Laughner, J. L., Roche, S., Kiel, M., Toon, G. C., Wunch, D., Baier, B. C., Biraud, S., Chen, H., Kivi, R., Laemmle, T., McKain, K., Quéhé, P.-Y., Rousogonous, C., Stephens, B. B., Walker, K., and Wennberg, P. O.: A New Algorithm to Generate a Priori Trace Gas Profiles for the GGG2020 Retrieval Algorithm, *Atmos. Meas. Tech.*, 16, 1121–1146, <https://doi.org/10.5194/amt-16-1121-2023>, 2023.
- Levenberg, K.: A Method for the Solution of Certain Non-Linear Problems in Least Squares, *Quart. J. Appl. Math.*, 2, 164–168, <https://doi.org/10.1090/qam/10666>, 1944.
- 15 Logan, J. A., Prather, M. J., Wofsy, S. C., and McElroy, M. B.: Tropospheric chemistry: A global perspective, *J. Geophys. Res.*, 86, 7210–7254, <https://doi.org/10.1029/JC086iC08p07210>, 1981.
- Lucchesi, R.: File Specification for GEOS-5 FP-IT (Forward Processing for Instrument Teams), Tech. rep., National Aeronautics and Space Administration, Global Modeling and Assimilation Office, NASA Goddard Spaceflight Center, Greenbelt, MD, USA, <https://ntrs.nasa.gov/citations/20150001438>, 2013.
- 20 Marquardt, D. W.: An Algorithm for Least-Squares Estimation of Nonlinear Parameters, *SIAM J. Appl. Math.*, 11, 431–441, <https://doi.org/10.1137/0111030>, 1963.
- Matsunaga, T. and Tanimoto, H.: Greenhouse gas observation by TANSO-3 onboard GOSAT-GW, in: *Sensors, Systems, and Next-Generation Satellites XXVI*, edited by Babu, S. R., Hélière, A., and Kimura, T., vol. 12264, p. 122640B, International Society for Optics and Photonics, The International Society for Optical Engineering (SPIE), <https://doi.org/10.1117/12.2639221>, 2022.
- 25

- Meister, C., Keim, C., Irizar, J., and Bauer, M.: Sentinel-5/UVNS Instrument: The Principle Ability of a Slit Homogenizer to Reduce Scene Contrast for Earth Observation Spectrometer, in: Proceedings of SPIE Volume 10423, Sensors, Systems, and Next-Generation Satellites XXI, p. 12, The International Society for Optical Engineering (SPIE), 2017.
- 30 Miller, C. E., Crisp, D., DeCola, P. L., Olsen, S. C., Randerson, J. T., Michalak, A. M., Alkhaled, A., Rayner, P., Jacob, D. J., Suntharalingam, P., Jones, D. B. A., Denning, A. S., Nicholls, M. E., Doney, S. C., Pawson, S., Boesch, H., Connor, B. J., Fung, I. Y., O'Brien, D., Salawitch, R. J., Sander, S. P., Sen, B., Tans, P., Toon, G. C., Wennberg, P. O., Wofsy, S. C., Yung, Y. L., and Law, R. M.: Precision Requirements for Space-Based $XC\text{O}_2$ Data, *J. Geophys. Res.*, 112, D10314, <https://doi.org/10.1029/2006JD007659>, 2007.
- 35 Moore III, B., Crowell, S. M. R., Rayner, P. J., Kumer, J., O'Dell, C. W., O'Brien, D., Utembe, S., Polonsky, I., Schimel, D., and Lemen, J.: The Potential of the Geostationary Carbon Cycle Observatory (GeoCarb) to Provide Multi-scale Constraints on the Carbon Cycle in the Americas, *Front. Environ. Sci.*, 17, 6, <https://doi.org/10.3389/fenvs.2018.00109>, 2018.
- Nakajima, M., Kuze, A., and Suto, H.: The current status of GOSAT and the concept of GOSAT-2, in: Sensors, Systems, and Next-Generation Satellites XVI, edited by Meynart, R., Neeck, S. P., and Shimoda, H., vol. 8533, p. 853306, International Society for Optics and Photonics, SPIE, <https://doi.org/10.1117/12.974954>, 2012.
- Nassar, R., Hill, T. G., McLinden, C. A., Wunch, D., Jones, D. B. A., and Crisp, D.: Quantifying CO_2 Emissions From Individual Power Plants From Space, *Geophys. Res. Lett.*, 44, 10,045–10,053, <https://doi.org/10.1002/2017GL074702>, 2017.
- 5 Nivitanont, J., Crowell, S., O'Dell, C., Burgh, E., McGarragh, G., O'Brien, D., and Moore, B.: Characterizing the Effects of Inhomogeneous Scene Illumination on Retrievals of Greenhouse Gases from a Geostationary Platform, in: AGU Fall Meeting, American Geophysical Union (AGU), San Francisco, CA, USA, 2019a.
- Nivitanont, J., Crowell, S. M. R., and Moore III, B.: A Scanning Strategy Optimized for Signal-to-Noise Ratio for the Geostationary Carbon Cycle Observatory (GeoCarb) Instrument, *Atmos. Meas. Tech.*, 12, 3317–3334, <https://doi.org/10.5194/amt-12-3317-2019>, 2019b.
- O'Brien, D. M. and Rayner, P. J.: Global Observations of the Carbon Budget 2. CO_2 Column From Differential Absorption of Reflected Sunlight in the $1.61 \mu\text{m}$ Band of CO_2 , *J. Geophys. Res.*, 107, 4354, <https://doi.org/10.1029/2001JD000617>, 2002.
- 10 O'Brien, D. M., Mitchell, R. M., English, S. A., and Costa, G. D.: Airborne Measurements of Air Mass from O₂ A-Band Absorption Spectra, *J. Atmos. Oceanic. Tech.*, 15, 1272–1286, [https://doi.org/10.1175/1520-0426\(1998\)015<1272:AMOAMF>2.0.CO;2](https://doi.org/10.1175/1520-0426(1998)015<1272:AMOAMF>2.0.CO;2), 1998.
- O'Brien, D. M., Polonsky, I., O'Dell, C., and Carheden, A.: Orbiting Carbon Observatory (OCO) Algorithm Theoretical Basis Document: The OCO Simulator, Tech. rep., Cooperative Institute for Research in the Atmosphere, Colorado State University, Fort Collins, Colorado, 15 USA, 2009.
- O'Brien, D. M., Polonsky, I. N., and Kumer, J. B.: Sensitivity of Remotely Sensed Trace Gas Concentrations to Polarisation, *Atmos. Meas. Tech.*, 8, 4917–4930, <https://doi.org/10.5194/amt-8-4917-2015>, 2015.
- O'Brien, D. M., Polonsky, I. N., Utembe, S. R., and Rayner, P. J.: Potential of a Geostationary geoCARB Mission to Estimate Surface Emissions of CO_2 , CH_4 and CO in a Polluted Urban Environment: Case Study Shanghai, *Atmos. Meas. Tech.*, 9, 4633–4654, 20 <https://doi.org/10.5194/amt-9-4633-2016>, 2016.
- O'Dell, C. W., Day, J. O., Pollock, R., Bruegge, C. J., O'Brien, D. M., Castano, R., Tkatcheva, I., Miller, C. E., and Crisp, D.: Preflight Radiometric Calibration of the Orbiting Carbon Observatory, *IEEE Trans. Geosci. Remote Sens.*, 49, 2438–2447, <https://doi.org/10.1109/TGRS.2016.2634023>, 2011.
- O'Dell, C. W., Connor, B., Bosch, H., O'Brien, D., Frankenberg, C., Castano, R., Christi, M., Eldering, D., Fisher, B., Gunson, M., McDuffie, J., Miller, C. E., Natraj, V., Oyafuso, F., Polonsky, I., Smyth, M., Taylor, T., Toon, G. C., Wennberg, P. O., and Wunch, D.: The 25

- ACOS CO₂ Retrieval Algorithm - Part 1: Description and Validation Against Synthetic Observations, *Atmos. Meas. Tech.*, 5, 99–121, <https://doi.org/10.5194/amt-5-99-2012>, 2012.
- O'Dell, C. W., Eldering, A., Wennberg, P. O., Crisp, D., Gunson, M. R., Fisher, B., Frankenberg, C., Kiel, M., Lindqvist, H., Mandrake, L., Nelson, A. M. V. N. R. R., Payne, G. B. O. V. H., Taylor, T. E., Wunch, D., Drouin, B. J., Smyth, F. O. A. C. J. M. M., Baker, D. F., Basu, S., Feng, F. C. S. M. R. C. L., Palmer, P. I., García, M. D. O. E., Griffith, D. W. T., Hase, F., Iraci, L. T., Kivi, R., Morino, I., Notholt, J., Petri, H. O. C., Roeh, C. M., Sha, M. K., Strong, K., Te, R. S. Y., Uchino, O., and Velasco, V. A.: Improved Retrievals of Carbon Dioxide from Orbiting Carbon Observatory-2 with the Version 8 ACOS algorithm, *Atmos. Meas. Tech.*, 11, 6539–6576, <https://doi.org/10.5194/amt-11-6539-2018>, 2018.
- Pascal, V., Buil, C., Loesel, J., Tauziede, L., Jouget, D., and Buisson, F.: An improved MicroCarb dispersive instrumental concept for the measurement of greenhouse gases concentration in the atmosphere, in: *International Conference on Space Optics — ICSO 2014*, edited by Sodnik, Z., Cugny, B., and Karafolas, N., vol. 10563, p. 105633K, International Society for Optics and Photonics, SPIE, <https://doi.org/10.1117/12.2304219>, 2017.
- Polonsky, I. N., O'Brien, D. M., Kumer, J. B., O'Dell, C. W., and the geoCARB Team: Performance of a Geostationary Mission, geoCARB, to Measure CO₂, CH₄ and CO Column-averaged Concentrations, *Atmos. Meas. Tech.*, 7, 959–981, <https://doi.org/10.5194/amt-7-959-2014>, 2014.
- Rayner, P. J. and O'Brien, D. M.: The Utility of Remotely Sensed CO₂ Concentration Data in Surface Source Inversions, *Geophys. Res. Lett.*, 28, 175–178, <https://doi.org/10.1029/2000GL011912>, 2001.
- Rayner, P. J., Law, R. M., and O'Brien, D. M.: Global Observations of the Carbon Budget 3. Initial Assessment of the Impact of Satellite Orbit, Scan Geometry, and Cloud on Measuring CO₂ from Space, *J. Geophys. Res.*, 107, 4557, <https://doi.org/10.1029/2001JD000618>, 2002.
- Reuter, M., Buchwitz, M., Schneising, O., Heymann, J., Bovensmann, H., and Burrows, J. P.: A Method for Improved SCIAMACHY CO₂ Retrieval in the Presence of Optically Thin Clouds, *Atmos. Meas. Tech.*, 3, 209–232, <https://doi.org/10.5194/amt-3-209-2010>, 2010.
- Reuter, M., Buchwitz, M., Schneising, O., Noël, S., Rozanov, V., Bovensmann, H., and Burrows, J.: A Fast Atmospheric Trace Gas Retrieval for Hyperspectral Instruments Approximating Multiple Scattering—Part 1: Radiative Transfer and a Potential OCO-2 XCO₂ Retrieval Setup, *Remote Sens.*, 9, 1159, <https://doi.org/10.3390/rs9111159>, 2017.
- Rienecker, M. M., Suarez, M. J., Todling, R., Bacmeister, J., Takacs, L., Liu, H. C., Gu, W., Sienkiewicz, M., Koster, R. D., Gelaro, R., Stajner, I., and Nielsen, J.: The GEOS-5 Data Assimilation System—Documentation of Versions 5.0.1, 5.1.0, and 5.2.0, Tech. rep., National Aeronautics and Space Administration, NASA Goddard Spaceflight Center, Greenbelt, MD, USA, <https://ntrs.nasa.gov/citations/20120011955>, 2008.
- Rienecker, M. M., Suarez, M. J., Gelaro, R., Todling, R., Bacmeister, J., Liu, E., Bosilovich, M. G., Schubert, S. D., Takacs, L., Kim, G.-K., Bloom, S., Chen, J., Collins, D., Conaty, A., da Silva, A., Gu, W., Joiner, J., Koster, R. D., Lucchesi, R., Molod, A., Owens, T., Pawson, S., Pegion, P., Redder, C. R., Reichle, R., Robertson, F. R., Ruddick, A. G., Sienkiewicz, M., and Woollen, J.: MERRA: NASA's Modern-Era Retrospective Analysis for Research and Applications, *J. Climate.*, 24, 3624–3648, <https://doi.org/10.1175/JCLI-D-11-00015.1>, 2011.
- Rodgers, C. D.: Retrieval of Atmospheric Temperature and Composition from Remote Measurements of Thermal Radiation, *Rev. Geophys.*, 14, 609–624, <https://doi.org/10.1029/RG014i004p00609>, 1976.
- Rodgers, C. D.: Information Content and Optimisation of High Spectral Resolution Remote Measurements, *Adv. Space. Res.*, 21, 361–367, [https://doi.org/10.1016/S0273-1177\(97\)00915-0](https://doi.org/10.1016/S0273-1177(97)00915-0), 1998.

- Rodgers, C. D.: *Inverse Methods for Atmospheric Sounding: Theory and Practice*, World Scientific Publishing Co. Pte. Ltd., 5 Toh Tuck Link, Singapore 596224, reprint edn., 2004.
- Rothman, L., Gordon, I. E., Barbe, A., Benner, D. C., Bernath, P. F., Birk, M., Boudon, V., Brown, L. R., Campargue, A., Champion, J.-P., Chance, K., Coudert, L. H., Dana, V., Devi, V. M., Fally, S., Flaud, J.-M., Gamache, R. R., Goldman, A., Jacquemart, D., Kleiner, I., 30 Lacome, N., Lafferty, W. J., Mandin, J.-Y., Massie, S., Mikhailenko, S. N., Miller, C. E., Moazzen-Ahmadi, N., Naumenko, O. V., Nikitin, A. V., Orphal, J., Perevalov, V. I., Perrin, A., Predoi-Cross, A., Rinsland, C. P., Rotger, M., Simeckova, M., Smith, M. A. H., Sung, K., Tashkun, S. A., Tennyson, J., Toth, R. A., Vandaele, A. C., and Auwera, J. V.: The HITRAN 2008 Molecular Spectroscopic Database, *J. Quant. Spectrosc. Radiat. Transfer.*, 110, 533–572, <https://doi.org/10.1016/j.jqsrt.2009.02.013>, 2009.
- Sellers, P. J., Schimel, D. S., Moore III, B., Liu, J., and Eldering, A.: Observing Carbon Cycle–Climate Feedbacks from Space, *Geophys. Res. Lett.*, 115, 7860–7868, <https://doi.org/10.1073/pnas.1716613115>, 2018. 35
- Shindell, D. T., Faluvegi, G., Stevenson, D. S., Krol, M. C., Emmons, L. K., Lamarque, J.-F., Pe tron, G., Dentener, F. J., Ellingsen, K., Schultz, M. G., Wild, O., Amann, M., Atherton, C. S., Bergmann, D. J., Bey, I., Butler, T., Cofala, J., Collins, W. J., Derwent, R. G., Doherty, R. M., Drevet, J., Eskes, H. J., Fiore, A. M., Gauss, M., Hauglustaine, D. A., Horowitz, L. W., Isaksen, I. S. A., Lawrence, M. G., Montanaro, V., M ller, J.-F., Pitari, G., Prather, M. J., Pyle, J. A., Rast, S., Rodriguez, J. M., Sanderson, M. G., Savage, N. H., Strahan, S. E., Sudo, K., Szopa, S., Unger, N., van Noije, T. P. C., and Zeng, G.: Multimodel Simulations of Carbon Monoxide: Comparison with Observations and Projected Near-future Changes, *J. Geophys. Res.*, 111, 24, <https://doi.org/10.1029/2006JD007100>, 2006.
- Sierk, B., Fernandez, V., B zy, J.-L., Meijer, Y., Durand, Y., Courr ges-Lacoste, G. B., Pachot, C., L scher, A., Nett, H., Minoglou, K., 5 Boucher, L., Windpassinger, R., Pasquet, A., Serre, D., and te Hennepe, F.: The Copernicus CO2M mission for monitoring anthropogenic carbon dioxide emissions from space, in: *International Conference on Space Optics — ICSO 2020*, edited by Cugny, B., Sodnik, Z., and Karafolas, N., vol. 11852, p. 118523M, International Society for Optics and Photonics, SPIE, <https://doi.org/10.1117/12.2599613>, 2021.
- Somkuti, P., O’Dell, C., Crowell, S., K hler, P., McGarragh, G., Cronk, H., and Burgh, E.: Solar-induced Chlorophyll Fluorescence from the Geostationary Carbon Cycle Observatory (GeoCarb): An Extensive Simulation Study, *Remote Sens. Environ.*, 263, 10 <https://doi.org/10.1016/j.rse.2021.112565>, 2021.
- Suto, H., Kataoka, F., Kikuchi, N., Knuteson, R. O., M., A. B., Haun, Buijs, H., Shiomi, K., Imai, H., and Kuze, A.: Thermal and Near-infrared Sensor for Carbon Observation Fourier Transform Spectrometer-2 (TANSO-FTS-2) on the Greenhouse gases Observing SATellite-2, *Atmos. Meas. Tech.*, 14, 2013–2039, <https://doi.org/10.5194/amt-14-2013-2021>, 2021.
- Taylor, T. E., O’Dell, C. W., O’Brien, D. M., Kikuchi, N., Yokota, T., Nakajima, T. Y., Ishida, H., Crisp, D., and Nakajima, T.: 15 Comparison of Cloud-Screening Methods Applied to GOSAT Near-Infrared Spectra, *IEEE Trans. Geosci. Remote Sens.*, 50, 75–88, <https://doi.org/10.1109/TGRS.2011.2160270>, 2012.
- Townshend, J. R. G.: *Improved Global Data for Land Applications*, IGBP Global Change Report no. 20, Tech. rep., The International Geosphere–Biosphere Programme (IGBP), Stockholm, Sweden, 1992.
- Veefkind, J. P., Aben, I., McMullan, K., F rster, H., de Vries, J., Otter, G., Claas, J., Eskes, H., de Haan, J., Kleipool, Q., van Weele, M., 20 Hasekamp, O., Hoogeveen, R., Landgraf, J., Snel, R., Tol, P., Ingmann, P., Voors, R., Kruizinga, B., Vink, R., Visser, H., and Levelt, P. F.: TROPOMI on the ESA Sentinel-5 Precursor: A GMES Mission for Global Observations of the Atmospheric Composition for Climate, Air Quality and Ozone Layer Applications, *Remote Sens. Environ.*, 120, 70–83, <https://doi.org/10.1016/j.rse.2011.09.027>, 2012.
- Wunch, D., Toon, G. C., Blavier, J.-F. L., Washenfelder, R. A., Notholt, J., Connor, B. J., Griffith, D. W. T., Sherlock, V., and Wennberg, P. O.: The Total Carbon Column Observing Network, *Phil. Trans. R. Soc. A*, 369, 2087–2112, <https://doi.org/10.1098/rsta.2010.0240>, 2011a.

- 1255 Wunch, D., Wennberg, P. O., Toon, G. C., Connor, B. J., Fisher, B., Osterman, G. B., Frankenberg, C., Mandrake, L., O'Dell, C., Ahonen, P., Biraud, S. C., Castano, R., Cressie, N., Crisp, D., Deutscher, N. M., Eldering, A., Fisher, M. L., Griffith, D. W. T., Gunson, M., Heikkinen, P., Keppel-Aleks, G., Kyrö, E., Lindenmaier, R., Macatangay, R., Mendonca, J., Messerschmidt, J., Miller, C. E., Morino, I., Notholt, J., Oyafuso, F. A., Rettinger, M., Robinson, J., Roehl, C. M., Salawitch, R. J., Sherlock, V., Strong, K., Sussmann, R., Tanaka, Thompson, D. R., Uchino, O., Warneke, T., and Wofsy, S. C.: A Method for Evaluating Bias in Global Measurements of CO₂ Total Columns from Space, *Atmos. Chem. and Phys.*, 11, 12 317–12 337, <https://doi.org/10.5194/acp-11-12317-2011>, 2011b.
- 1260 Wunch, D., Wennberg, P. O., Gregory Osterman and, B. F., Naylor, B., Roehl, C. M., O'Dell, C., Mandrake, L., Viatte, C., Kiel, M., Griffith, D. W. T., Deutscher, N. M., Velazco, V. A., Notholt, J., Warneke, T., Petri, C., Maziere, M. D., Sha, M. K., Sussmann, R., Rettinger, M., Pollard, D., Robinson, J., Morino, I., Uchino, O., Hase, F., Blumenstock, T., Feist, D. G., Arnold, S. G., Strong, K., Mendonca, J., Kivi, R., Heikkinen, P., Iraci, L., Podolske, J., Hillyard, P. W., Kawakami, S., Dubey, M. K., Parker, H. A., Sepulveda, E., García, O. E., Te, Y., Jeseck, P., Gunson, M. R., Crisp, D., and Eldering, A.: Comparisons of the Orbiting Carbon Observatory-2 (OCO-2) X_{CO₂} measurements with TCCON, *Atmos. Meas. Tech.*, 10, 2209–2238, <https://doi.org/10.5194/amt-10-2209-2017>, 2017.
- 1265 Xi, X., Natraj, V., Shia, R. L., Luo, M., Zhang, Q., Newman, S., Sander, S. P., and Yung, Y. L.: Simulated Retrievals for the Remote Sensing of CO₂, CH₄, CO, and H₂O from Geostationary Orbit, *Atmos. Meas. Tech.*, 8, 4817–4830, <https://doi.org/10.5194/amt-8-4817-2015>, 2015.
- 1270 Yang, D., Liu, Y., Cai, Z., Chen, X., Yao, L., and Lu, D.: First Global Carbon Dioxide Maps Produced from TanSat Measurements, *J. Adv. Atmos. Sci.*, 35, 621–623, <https://doi.org/10.1007/s00376-018-7312-6>, 2018.
- Yokota, T., Eguchi, Y. Y. N., Ota, Y., Tanaka, T., Watanabe, H., and Maksyutov, S.: Global Concentrations of CO₂ and CH₄ Retrieved from GOSAT: First Preliminary Results, *Sci. Online Lett. Atmosphere*, 5, 160–163, <https://doi.org/10.2151/sola.2009-041>, 2009.
- 1275 Yoshida, Y., Ota, Y., Eguchi, N., Kikuchi, N., Nobuta, K., Tran, H., Morino, I., and Yokota, T.: Retrieval Algorithm For CO₂ and CH₄ Column Abundances from Short-Wavelength Infrared Spectral Observations by the Greenhouse Gases Observing Satellite, *Atmos. Meas. Tech.*, 4, 717–734, <https://doi.org/10.5194/amt-4-717-2011>, 2011.